Article

W–CeO$_2$ Core–Shell Powders and Macroscopic Migration of the Shell via Viscous Flow during the Initial Sintering Stage

Haitao Yang [1,2,†], **Ningfei Zhang** [1,†], **Chan Wang** [3] **and Qingyu Hou** [1,*]

[1] School of Metallurgical Engineering, Anhui University of Technology, Maanshan 243032, China; ngyanghaitao@163.com.cn (H.Y.); zhangningfei@ahut.edu.cn (N.Z.)
[2] Nanjing Iron and Steel Co., Ltd., Nanjing 210035, China
[3] Deyang Sanhuan Technology Co., Ltd., Deyang 618000, China; 18855576276@163.com
[*] Correspondence: qingyuhou@hotmail.com or houqingyu@ahut.edu.cn; Tel./Fax: +86-555-2311570
[†] These authors contributed equally to this work.

Abstract: To retard the mutual contact of W grains to inhibit their growth, in this study, CeO$_2$·2H$_2$O was first coated on the surface of pure W (undoped) particles by a weight percentage of 4% using a wet chemical method to prepare CeO$_2$·2H$_2$O-doped W-based (doped) powders, with W particles as the core and CeO$_2$·2H$_2$O as the shell (W–CeO$_2$·2H$_2$O core–shell structure), without hydrogen reduction treatment. The undoped and doped powders were subsequently sintered using a spark plasma sintering (SPS) apparatus to fabricate bulk materials. The macroscopic migration of the CeO$_2$ shell in the core–shell W–CeO$_2$ system via viscous flow during the initial sintering stage was studied through simulations and experiments. The results showed that a core–shell structure with W particles as the core and CeO$_2$·2H$_2$O as the shell was successfully prepared. The doped powder contained approximately 3.97% CeO$_2$, consistent with the designed content of 4%. The shell materials migrated among the selected four sintered powders, filling the pores and contributing to the improvement in the relative density of the sintered bulk.

Keywords: tungsten; CeO$_2$-doped; core–shell; viscous flow; filling effect

1. Introduction

Tungsten (W) has the potential for application in the plasma-facing material (PFM) used for thermonuclear fusion power reactors due to its possession of a high melting point, high thermal conductivity, high sputtering threshold, high strength at elevated temperatures, low thermal expansion coefficient, and low tritium inventory [1,2]. Therefore, W has been successfully applied for manufacturing the diverter of the International Thermonuclear Experimental Reactor (ITER) [3]. The main factors restricting the application of polycrystalline W, which is commonly used in practice, include brittleness or embrittlement problems (low toughness), including low-temperature brittleness, recrystallization embrittlement, and irradiation embrittlement [4–6]. The doping of rare earth oxides (REOs), such as La$_2$O$_3$ and Y$_2$O$_3$, in polycrystalline W to prepare W-based bulk materials is one of the effective ways to improve these problems because they have a hindering effect on grain growth and grain boundary sliding during the preparation and application of the bulk materials and an inhibiting effect on crack initiation and propagation in these bulk materials [7–9]. The improvement effect of doped REO on the above-mentioned problems of these bulk materials is attributed to their grain refinement and intragranular or intergranular strengthening effects, especially the grain refinement effect, generated during the preparation and application of these bulk materials [7–9].

Due to the fact that the W-based bulk materials used for PFMs are commonly prepared by sintering W-based powders into sintered bulk materials followed by hot working, the characteristics of the W-based powders used for sintering, which are determined mainly by the preparation method and path, are some of the main factors limiting whether W-based

bulk materials after hot working have fine W grains. The preparation of REO-doped W-based powders mainly includes mechanical alloying and wet chemical methods. With the mechanical alloying method, the preparation of REO-doped W-based powders involves the deformation, broken, and mixing of pure W and REO powders via mechanical grinding in a ball-milling tank [10,11]. Mechanical alloying can easily introduce impurities and result in uneven coating. In addition, there are also methods such as vapor-phase deposition, sol–gel, electroplating, etc. The sol–gel method is complicated, requiring strict control of reaction conditions, and the product might contain impurities. The electroplating method is costly, prone to environmental pollution, and involves complex operations. With the wet chemical method, the preparation of REO-doped W-based powders characterized by a core–shell structure with REO particles as the core and W particles as the shell (REO–W) involves the precipitation of tungsten oxides on the surfaces of the REO particles in a reaction vessel containing the main salt tungsten salt solution and the reducing agent solution, which is followed by suction filtration, drying, and hydrogen reduction or freeze-drying treatment [12]. The other path for preparing REO-doped W-based powders characterized by a mixture of tungsten particles and REO particles using a wet chemical method involves the co-deposition of tungsten oxides and REO particles in a reaction vessel containing a tungsten salt solution, a rare earth salt solution, and a reducing agent solution, followed by suction filtration, drying, and hydrogen reduction [13–15]. Contact between W particles or W shells is inevitable when REO-doped W-based powders are prepared using the above-mentioned path, increasing the coalescence trend of W particles or W shells in the subsequent sintering process, which is unfavorable for obtaining fine W grains.

Compared to the above-mentioned REO-doped W-based powders, if REO-doped W-based powders, characterized by a core–shell structure with W particles as the cores and REO as the shells, could be prepared, it would reduce the coalescence trend of W particles and the growth trend of W grains during the sintering process, which could contribute to obtaining sintered bulk materials with fine W grains. The sintering delay effect of oxide shells on metal cores has also been proposed in other studies [16,17]. Our recent investigation also indicated that La_2O_3 shells have a sintering delay effect on W cores for La_2O_3-doped W-based powders with W particles as the core and La_2O_3 as the shell (core–shell W–La_2O_3), which is one of the reasons that the W grain size of e La_2O_3-doped W-based bulk material is smaller than that of La_2O_3-free W-based bulk material [18]. Although the sintering delay effect of La_2O_3 shells on W cores in the initial stage of sintering was explained using a two-ball sintering neck model and was verified by experiments, the macroscopic migration mechanisms of La_2O_3 shells, which determine the sintering delay effect of the La_2O_3 shell on the W core, has not been studied.

Therefore, in this work, $Ce(OH)_4$ ($CeO_2 \cdot 2H_2O$ [19–21]), the precursor of rare earth oxide CeO_2, was first coated on the surface of pure tungsten (undoped) particles at a weight percentage of 4% using a wet chemical method to prepare $CeO_2 \cdot 2H_2O$-doped W-based (doped) powders with W particles as the core and $CeO_2 \cdot 2H_2O$ as the shell (W–$CeO_2 \cdot 2H_2O$ core–shell). When the doped powders were sintered, W–$CeO_2 \cdot 2H_2O$ was expressed as W–CeO_2 because $CeO_2 \cdot 2H_2O$ dehydrated to form CeO_2 when the sintering temperature increased to about 340 °C [22]. The undoped and doped powders were then sintered using a spark plasma sintering (SPS) apparatus to fabricate bulk materials. The characteristics of the undoped and doped powders and their sintered bulk materials were first analyzed. The macroscopic migration of the CeO_2 shell in the core–shell W–CeO_2 system via viscous flow in the initial stage of sintering was then studied through simulation and experiments.

2. Experimental

2.1. Materials and Reagents

The purity and size of the tungsten (W) powders to be used to prepare W-based powders were, respectively, about 99.95% and 2–3 μm. All the chemicals and reagents used in the study, including cerium nitrate hexahydrate ($Ce(NO_3)_3 \cdot 6H_2O$), sodium hydroxide

(NaOH), polyethylene glycol ($C_8H_{14}O_4$), stannic chloride (SnCl), and hydrochloric acid (HCl), were of analytical grade.

2.2. Synthesis of Core–Shell Powders

The core–shell W–$CeO_2 \cdot 2H_2O$ powders, with a $CeO_2 \cdot 2H_2O$ content corresponding to 4 wt.% (denoted as doped powders), were synthesized through a wet chemical process using W powders, $Ce(NO_3)_3 \cdot 6H_2O$, NaOH, and $C_8H_{14}O_4$. At first, the pretreated W powders (denoted as undoped powders) were obtained from pure W powders by roughening with 3% HCl for 720 min, sensitizing and activating with 30 g/L SnCl and 5% HCl for 60 min, washing with deionized water and anhydrous ethanol in a vacuum glove chamber, followed by drying at 80 °C for 720 min in a vacuum drying oven. Then the main salt $Ce(NO_3)_3 \cdot 6H_2O$, the stabilizer and dispersant $C_8H_{14}O_4$, and the reducing agent and pH regulator NaOH were dissolved in deionized water to prepare solutions with concentrations of 3.4 g/L, 1.6g/L, and 10%, respectively. Mechanical stirring and ultrasonic treatment were carried out throughout the whole process. The main salt solution and the stabilizer and dispersant solution were sequentially added into a reactor and mixed for 30 min. Subsequently, pretreated W powders at a concentration of 16 g/L were added into the mixture solution and left to mix for an additional 30 min. Finally, the reducing agent and pH regulator, 10%NaOH, was added dropwise into the formed suspension at a concentration of 10 mL/L, inducing a chemical precipitation reaction on the surfaces of the pretreated W powders in the reactor for 20 min, forming $CeO_2 \cdot 2H_2O$-doped W-based powders (W–$CeO_2 \cdot 2H_2O$ core–shell) with W as the cores and $CeO_2 \cdot 2H_2O$ as the shells. Mechanical stirring and ultrasonic treatment were maintained throughout the whole process. During the reaction, the pH of the solution was controlled within the range of 10.28–12.00 by adjusting the amount of NaOH solution. The temperature of the reaction solution increased from room temperature to about 80 °C due to the exothermic nature of the reaction, as well as the stirring and ultrasonic treatment in the reactor. The collected doped powders were washed six times with deionized water and anhydrous ethanol in a vacuum glove chamber and then dried oven at 80 °C for 720 min.

2.3. Dehydration Temperature of the Shells

To formulate the sintering process, the dehydration temperature of the $CeO_2 \cdot 2H_2O$ shells in the obtained W–$CeO_2 \cdot 2H_2O$ core–shell powders was first determined by thermogravimetric and differential scanning calorimeter (TG–DSC) analysis. This analysis was conducted using a Netzsch STA449F3 thermogravimetric analyzer. The sample was heated from room temperature to 1200 °C in an Al_2O_3 crucible under a nitrogen atmosphere, with a heating rate of 20 °C/min.

2.4. Sintering of Powders

The undoped and doped powders were first, respectively, loaded into graphite modules lined internally with thin graphite sheets (~0.10 mm thick) and wrapped externally with a carbon blanket. The modules were then fixed in a spark plasma sintering (SPS) apparatus (SPS-III, Shanghai Chenhua Science Technology Corp., Shanghai, China). Once the vacuum level in the SPS apparatus reached about 3 Pa, a uniaxial pressure of about 3 MPa was applied to the powder bed prior to sintering. The maximum sintering temperature was 1800 °C, and a three-step sintering process was applied, as seen in Figure 1a, which provided the time–temperature and time–uniaxial pressure transformation diagrams of the sintering process. All sintering processes were conducted under vacuum conditions to prevent oxidation.
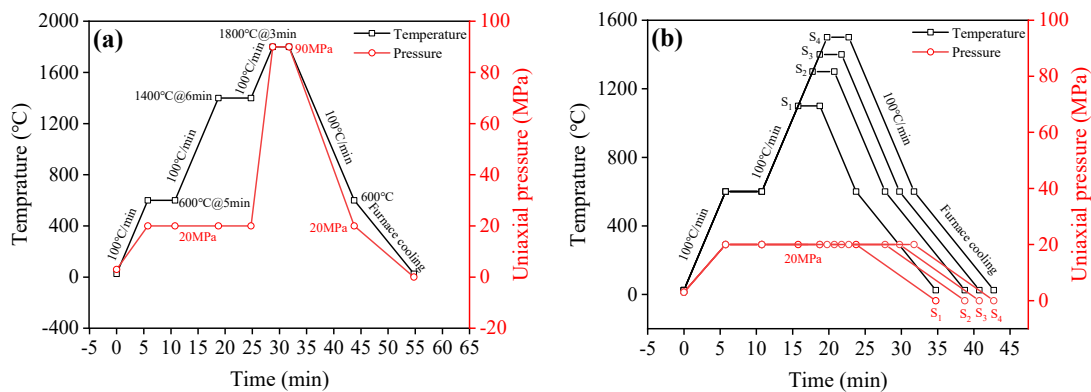
Figure 1. The time–temperature and time–uniaxial pressure transformation diagram of the sintering process: (**a**) for undoped and doped powders by the maximum sintering temperature of 1800 °C; (**b**) for doped powders by the maximum sintered temperatures of 1100 °C (S_1), 1300 °C (S_2), 1400 °C (S_3), and 1500 °C (S_4), respectively.

The first step of the sintering process involved heating the samples to 600 °C at a rate of 100 °C/min, followed by a dwell time of 5 min, during which the pressure increased from about 3 MPa to 20 MPa. During this stage, the $CeO_2 \cdot 2H_2O$ shells in the $W–CeO_2 \cdot 2H_2O$ core–shell powders dehydrated to form CeO_2 and H_2O(g) (with the dehydration temperature determined to be between 208 and 355 °C by TG/DSC analysis shown in following), resulting in the formation of $W–CeO_2$ core–shell powders. Moreover, the H_2O(g) produced from the dehydration and the residual gases in the undoped and doped powders were released, which contributed to avoiding the oxidation of W in the subsequent sintering steps. The second step involved heating the samples to 1400 °C at a rate of 100 °C/min under a pressure of 20 MPa, followed by a dwell time of 6 min to further release the residual gases in the undoped and doped powders. The third step involved heating the samples to 1800 °C at a rate of 100 °C/min, followed by a dwell time of 3 min, during which the pressure increased from 20 MPa to 90 MPa. After sintering, the bulk materials were cooled from the maximum sintering temperature of 1800 °C to 600 °C, and then the sintering apparatus was turned off to allow the bulk materials to cool to room temperature. During cooling, the uniaxial pressure was reduced from 90 MPa to 20 MPa as the temperature decreased to 600 °C and then to 0 MPa as the temperature decreased from 600 °C to room temperature.

In addition, the time–temperature and time–uniaxial pressure transformation diagrams for the doped powders sintered at maximum temperatures of 1100 °C (S_1), 1300 °C (S_2), 1400 °C (S_3), and 1500 °C (S_4) were also provided to show the macroscopic migration characteristics of the CeO_2 shells during sintering, as shown in Figure 1b. The procedures for the sintering processes shown in Figure 1b were similar to those shown in Figure 1a. The primary differences between Figures 1b and 1a were the maximum sintering temperature, the highest uniaxial pressure, and the lowest unloading pressure.

2.5. Microstructure Characterizations

The morphology and phase compositions of the undoped and doped powders were investigated using a field-emission scanning electron microscope (SEM, TESCAN MIRA3) with an energy dispersive X-ray spectrometer (EDX, Oxford, UK) and an X-ray diffractometer (XRD) operating with Cu Kα radiation. The phase compositions of the doped powders were also characterized by an X-ray photoelectron spectrometer (XPS, Escalab250Xi) with Al Kα (1486.6 eV) radiation under a vacuum pressure below 10^{-8} Torr. To maintain the original state of the doped powders, argon ion sputtering cleaning was not performed before the XPS measurement. For XPS measurement, the powders were laid flat on a substrate with an area of 400 μm^2, and the tested points were randomly selected for scanning and determination. Initially, a survey scan was recorded, followed by high-resolution scans

of the Ce3d, W4f, and O1s regions. The C1s peak, with a binding energy of about 285.09 eV, was used for internal calibration of the binding energies. All high-resolution spectra were fitted using a Gaussian–Lorentzian function after linear background subtraction, with position constraints set according to Moulder [23]. Peak identifications were referenced against the NIST XPS database. The core–shell structure of the doped powders was verified using SEM and EDX on the cross-section of a doped particle prepared by mechanical grinding and polishing.

The microstructure and composition of the sintered bulk materials were studied using SEM, EDX, and electron backscatter diffractometer (EBSD). The EBSD data were processed and analyzed using the EBSD analysis software by Channel 5. The sizes of the undoped and doped powders, as well as the porosity of the sintered bulk materials, were estimated from SEM micrographs taken at various locations on a specimen using the image analyzing software of ImageJ. Ten SEM images were used to perform a statistical analysis.

3. Characteristics of the Doped Powders and the Shells

3.1. Morphology and Phase Composition of the Doped Powders

To clarify the morphology and phase composition of the doped powders, the morphology and phase composition of the undoped powders were first analyzed, as shown in Figure 2. As could be seen from Figure 2a, the quasi-spherical W particles with a size of 1.6 ± 0.7 μm were confirmed. A magnified image of a selected W particle from Figure 2a indicated that the surface of the W particle possessed pits shown in Figure 2b, which facilitated the deposition of reaction products on its surface by the wet chemical method. Acid was used during both the roughening, sensitizing, and activating stages of the pretreated W powders, which was a lengthy process. Consequently, the surface of the W particles possessed pits during the acid etching process at the pretreatment stage. It could be confirmed from the XRD pattern of the undoped powders that the particles shown in Figure 2a,b were mainly composed of W phase, as shown in Figure 2c. In addition, the WO_x (x = 2–3) phase was identifiable in the undoped powders despite the high-purity W powders being selected. This might stem from the commercial W powders or the inevitable oxidation of W particles during the preparation process. The extremely low diffraction peak characteristics of the WO_x phase indicated that its content in the undoped powders was extremely low.

When the undoped powders were immersed in a mixed solution mainly containing $Ce(NO_3)_3 \cdot 6H_2O$, NaOH, and $C_8H_{14}O_4$, etc., reaction products were deposited in the pits located on the surface of W particles. This could be confirmed by the absence of pits (pits being a typical characteristic of the surface of W particles in the pretreated undoped powders) on the surface of W particles in the doped powders, as shown in Figure 3a,b. Therefore, doped powders were obtained. The evidence that the particle size of the doped powders (2.1 ± 1.0 μm, Figure 3a) was larger than that of the undoped powders confirmed that some reaction products deposited on the surface of the W particles. The EDX mappings of one of the doped particles shown in Figure 3b, indicated that the deposits were composed mainly of W, Ce, and O elements, as shown in Figure 3c–e. The distribution of Ce and O elements on the surface of the W particle was relatively dense. However, based on the distribution uniformity of Ce and O, it could be proposed that the deposit did not have the continuous characteristic of a complete film, similar to the shell oxide characteristics of most metal–oxide core–shell structures prepared by wet chemical methods [17,24–26].

The XRD pattern of the doped powders, shown in Figure 3f, indicates that the doped powders are composed of W and $CeO_2 \cdot 2H_2O$. This confirms that the Ce-rich and O-rich phase shown in Figure 3a,b was $CeO_2 \cdot 2H_2O$, which was prepared successfully when the undoped powders were immersed in the mixed solution mainly containing $Ce(NO_3)_3 \cdot 6H_2O$, NaOH, and $C_8H_{14}O_4$ etc. However, the WO_x phase could not be indexed in the doped powders by XRD analysis shown in Figure 3f. This might be attributed to its low content in the doped powders. The main reason was that the content of WO_x in the pretreated W powders (undoped powders) was relatively low, and the distribution of the deposits in the

pits on the surface of the pretreated W powders further reduced its probability of being detected by XRD.
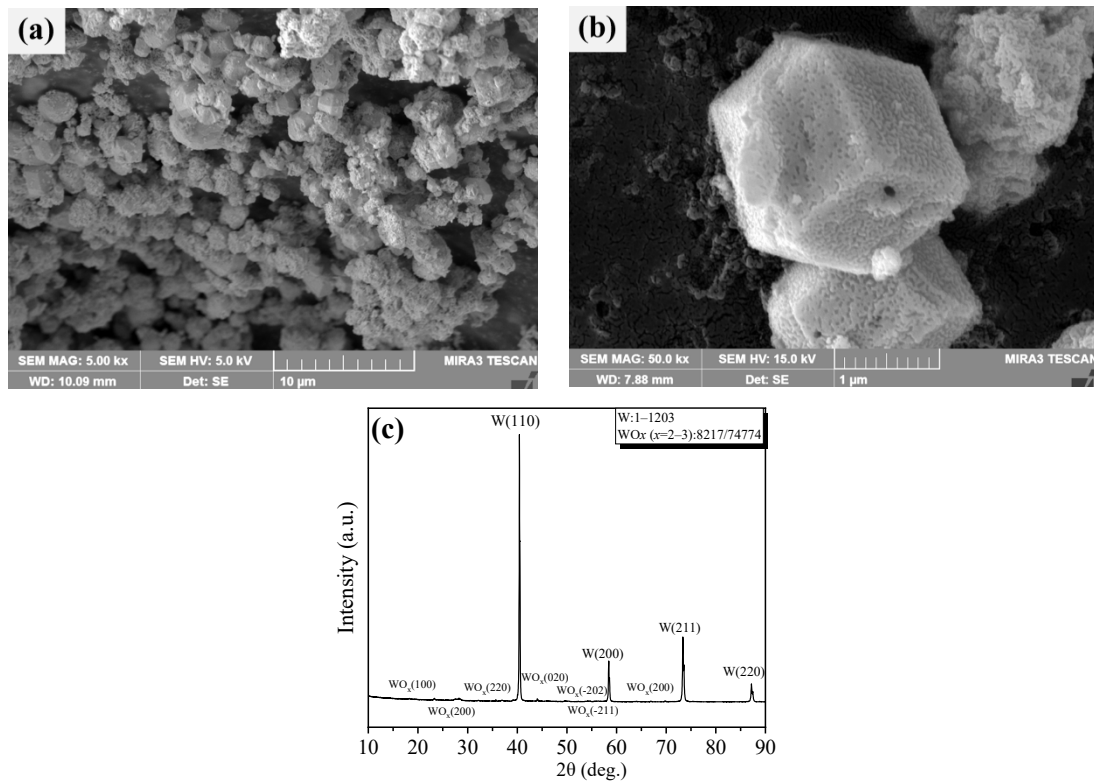

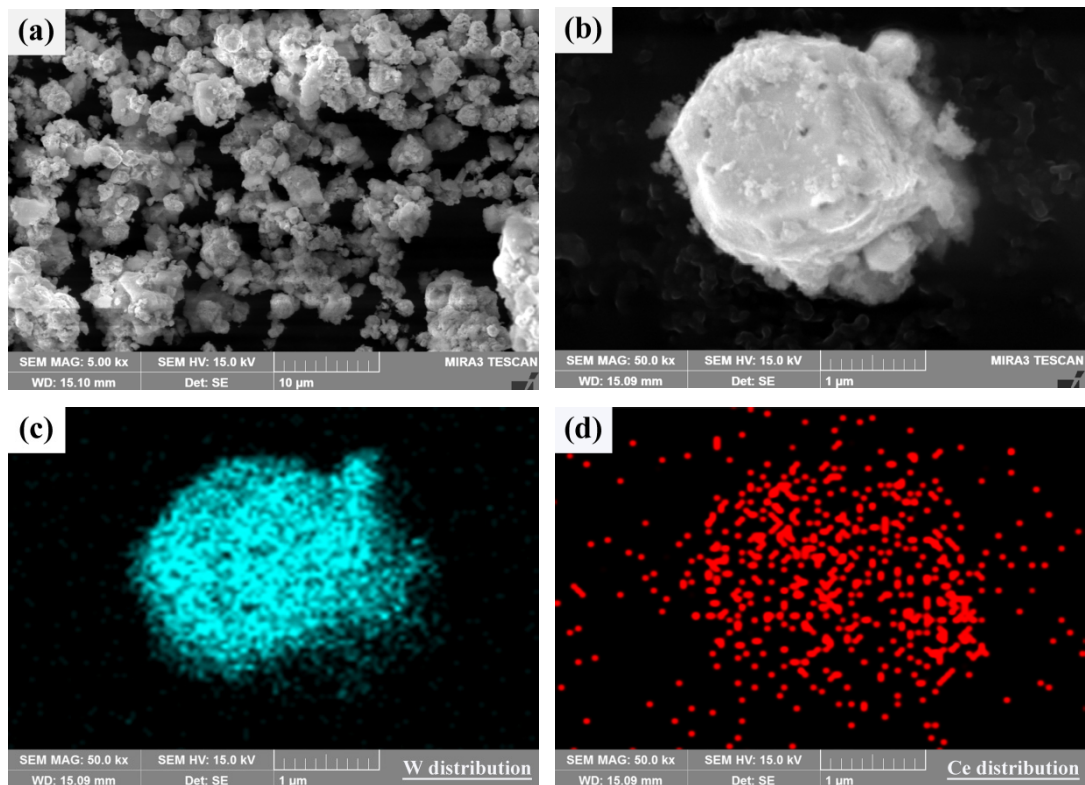**Figure 2.** SEM characteristics of the undoped powders: (**a**) morphology and size; (**b**) pits on the surface of the powder; (**c**) XRD pattern.
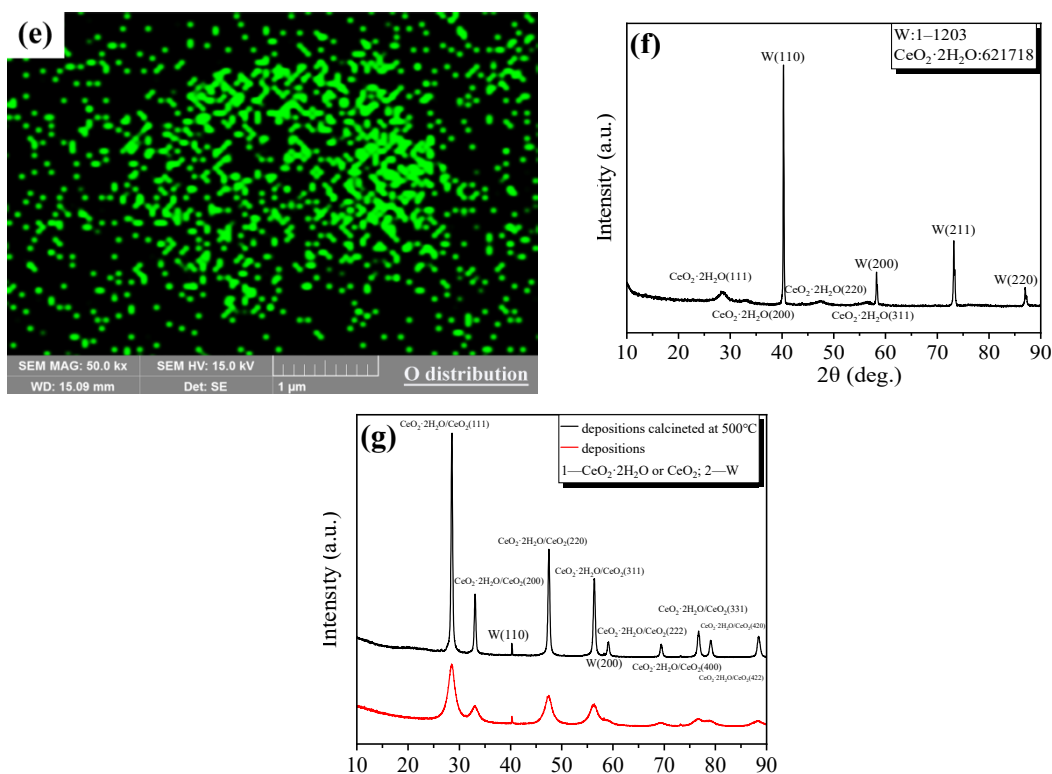

Figure 3. *Cont.*

Figure 3. SEM characteristics of the doped powders: (**a**) morphology; (**b**) one of the doped powders and its EDX mapping (**c**–**e**); (**f**) XRD pattern; (**g**) XRD pattern of the depositions before and after calcination.

It could also be seen from Figure 3f that the XRD peaks corresponding to the $CeO_2 \cdot 2H_2O$ phase in the doped powders had broad and amorphous-like characteristics. Balasubramanian et al. [27,28] proposed that a disordered form of hydrous cerium oxide ($CeO_2 \cdot 2H_2O$ [19–21]) might be more accurately represented as $Ce(OH)_4$. The observed broad and amorphous-like XRD peaks of $CeO_2 \cdot 2H_2O$ were attributed to its higher structural disorder, which led to such diffraction patterns. Upon the release of H_2O, crystallization characteristics occurred [27,28]. Therefore, the chemical formulation of $Ce(OH)_4$ might be incorrect, and the more appropriate designation should be hydrous cerium oxide [27,28], i.e., $CeO_2 \cdot 2H_2O$, which was consistent with the reported data [19–21].

The broad and amorphous-like characteristics of $CeO_2 \cdot 2H_2O$, along with its transformation to a crystalline structure, were further confirmed by the XRD analysis of the deposits of $CeO_2 \cdot 2H_2O$ prepared by the wet chemical method before and after calcination at 500 °C, as shown in Figure 3g. The XRD patterns revealed that the diffraction peaks associated with $CeO_2 \cdot 2H_2O$ transformed from broad and amorphous-like to typical crystalline structures upon the release of H_2O during calcination at 500 °C. This result provided evidence that $CeO_2 \cdot 2H_2O$ had an amorphous-like structure and would crystallize after dehydration [27,28]. The presence of a small amount of W in the XRD patterns shown in Figure 3g was attributed to residual W resulting from the separation process of $CeO_2 \cdot 2H_2O$ from the W–$CeO_2 \cdot 2H_2O$ core–shell powders.

The chemical compositions and phase characteristics of the doped powders were further confirmed by XPS analysis, as shown in Figure 4. The survey spectra of the doped powders shown in Figure 4a revealed that Ce 3d, O 1s, W 4p, C 1s, Ce 4p, Ce 4d, W 5p, and W 4f spectra. The spectra for Ce 3d, W 4f, and O 1s were, respectively, deconvoluted, as shown in Figure 4b–d.
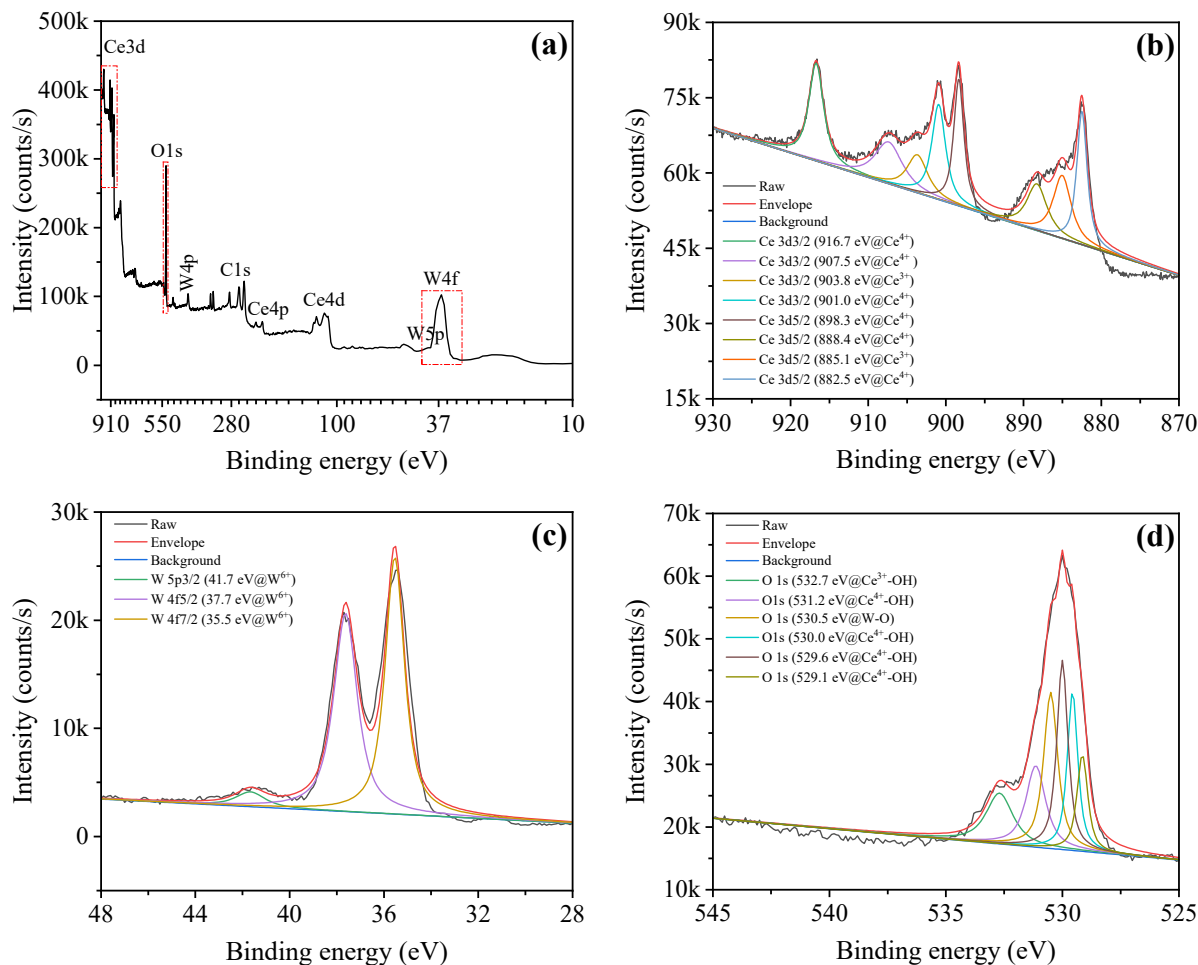
Figure 4. XPS spectra for the doped powders: (**a**) survey spectra; (**b**) Ce 3d3/2 and Ce 3d5/2 for Ce^{4+} and Ce^{3+}; (**c**) W 5p3/2 W 4f5/2 and W 4f7/2 for W^{6+}; (**d**) O 1s for Ce^{3+}-OH, Ce^{4+}-OH, and W-O: indicating $CeO_2 \cdot 2H_2O$, $Ce(OH)_3$, and WO_3 phases were detected from the W-based powders prepared by wet chemical method using XPS.

The Ce 3d spectra were deconvoluted into eight peaks using a least-square curve fitting method with a mixture of Gaussian and Lorentzian functions on a linear background, as shown in Figure 4b. These spectra distinguished two regions by Ce 3d3/2 and Ce 3d5/2. Six peaks at binding energy (BE) of about 916.7 eV, 907.5 eV, 901.0 eV, 898.3 eV, 888.4 eV, and 882.5 eV, and two peaks at the BE of about 903.8 eV and 885.1 eV were attributed to the Ce^{4+} and Ce^{3+} states, respectively. This agreed well with the reported spectra [29–32].

The W 4f spectra were deconvoluted into three peaks using the same curve fitting method as described above, as shown in Figure 4c. Two peaks at the BE of about 37.7 eV and 35.5 eV could be assigned to W^{6+} [33,34]. Another peak, characterized by a small and broad feature at a BE of about 41.7 eV, was attributed to the contribution of W 5P3/2 [34,35], which could also be assigned to W^{6+} [34,35].

The O 1s spectra were deconvoluted to six peaks using the same curve fitting method as described above shown in Figure 4d. Four peaks at the BE of about 531.2 eV, 530.0 eV, 529.6 eV, and 529.1 eV, along with one peak characterized by a small and broad feature at a BE of about 532.7 eV, were attributed to Ce^{4+}–OH and Ce^{3+}–OH [30–32,36]. Another peak, at a BE of about 530.5 eV, corresponded to W^{6+} [33,34].

Therefore, it could be proposed from Figure 4b–d $Ce(OH)_4$ ($CeO_2 \cdot 2H_2O$ [19–21]), $Ce(OH)_3$, and WO_3 were present in the doped powders. It was predicted by the amount and intensity of $CeO_2 \cdot 2H_2O$ and $Ce(OH)_3$ peaks that $CeO_2 \cdot 2H_2O$ content was significantly higher than that of $Ce(OH)_3$. Although W was the main phase in the doped powder,

its presence could not be determined in the XPS spectrum. As could be obtained from Figures 2 and 3, the coating effect of the deposits and WO_x on W powders was the main reason the W phase was difficult to detect by XPS analysis. This result further indicated that the deposits (shell) on the surface of W particles (core) were not a continuous thin film but rather distributed as granules on the surface of the W core, resulting in a porous shell. Otherwise, detecting the presence of the WO_x phase coated by the shell using XPS, which had a detection depth limited to the nanoscale, would be difficult. This conclusion was corroborated by the fact that the shell in metal–metal–oxide core–shell powders prepared by the wet chemical method exhibited porous characteristics [17,24].

In conclusion, as could be seen in Figure 4, the coating was mainly composed of $CeO_2 \cdot 2H_2O$ and a small amount of $Ce(OH)_3$. At lower heating temperatures, dehydration reactions would occur, forming oxides as shown in Equations (1) and (2). To further illustrate the dehydration characteristics of the coating during the heating process, the weight loss and endothermic and exothermic characteristics of the coating were investigated using TG–DSC from room temperature to 1100 °C, as shown in Figure 5. Two weight loss steps were observed within the temperature ranges of about 28–205 °C and 205–370 °C, with no obvious weight loss above 370 °C.

$$CeO_2 \cdot 2H_2O \rightarrow CeO_2 + 2H_2O \tag{1}$$

$$2Ce(OH)_3 \rightarrow Ce_2O_3 + 3H_2O \tag{2}$$

Figure 5. Dehydration characteristics of the doped powders determined by thermal analysis.

The first weight loss (TG), with a maximum rate (DTG) of about 0.24 wt.%/min at about 63 °C, was attributed to the loss of water from powders moistened by exposure to air, amounting to about 1.20%. The endothermic characteristic indicated by the red dotted lines in the DSC curve provided evidence that this weight loss was because of the release of water from the moistened powders. The second weight loss (TG), with a maximum rate (DTG) of about 0.16 wt.%/min at about 279 °C, was ascribed to the loss of water in $CeO_2 \cdot 2H_2O$ and $Ce(OH)_3$, totaling about 0.69 wt.%. The water loss of about 0.69 wt.% corresponded to the calculated content of H_2O in $CeO_2 \cdot 2H_2O$ from the doped powders based on Equation (1), further verified the above predictions that the pyrolysis water from $Ce(OH)_3$ was negligible compared to that from $CeO_2 \cdot 2H_2O$. This confirmed that $CeO_2 \cdot 2H_2O$ was the main deposit in the mixed aqueous solution, as indicated in Figure 4b. Therefore, it could be proposed that the exothermic peak with a maximum at about 288 °C in the DSC curve for the second weight loss could be regarded as the pyrolysis water from $CeO_2 \cdot 2H_2O$. The result was similar to the data indicating that $CeO_2 \cdot 2H_2O$ dehydrated at about 340 °C [22]. The release of pyrolysis water from $CeO_2 \cdot 2H_2O$ was accompanied by the breaking of the binding bonds, resulting in the release of heat and, thus, the exothermic peak on the DSC curve.

Therefore, the results shown in Figure 5 indicated that the content of water in $CeO_2 \cdot 2H_2O$ of the doped powders was about 0.69 wt.%. Based on a simple calculation using the molar mass of elements in one phase, the contents of $CeO_2 \cdot 2H_2O$ and CeO_2 in the doped powders were, respectively, about 3.99 wt.% and 3.30 wt.%, which could also be confirmed by the data obtained from EBSD analysis, as shown in Figure 6a.
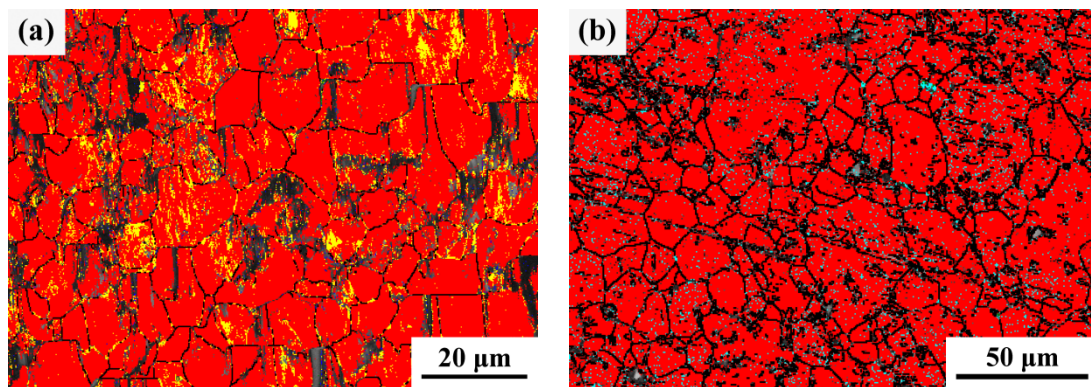

Figure 6. EBSD phase distribution results of the sintered bulk materials (obtained using an EBSD analysis post-processing software of Channel 5, the black was W grain boundaries, the red was W, the yellow was CeO_2, the blue was Ce_2O_3, the green was WO_3, the aqua was $WO_{2.96}$, and the gray and dark was zero solution points): (**a**) from doped powders; (**b**) from undoped powders.

As indicated by Figures 3 and 4, the shell in the obtained core–shell structure was mainly composed of $CeO_2 \cdot 2H_2O$ and a small amount of $Ce(OH)_3$. This composition could also be indirectly verified by the EBSD phase composition result of the bulk from the doped powders sintered at 1800 °C using the sintering process shown in Figure 1a, as shown in Figure 6a. For comparison, the EBSD phase analysis result of the bulk from the undoped powders sintered using the same process was illustrated in Figure 6b.

It could be obtained from Figure 6a that the sintered bulk from the doped powders was composed of about 75.58%W (red), 6.86%CeO_2 (yellow), 0.58%Ce_2O_3 (blue), 0.07%WO_3 (green), and 16.91% zero solution points (gray and dark), expressed in volume/area percentage (vol.%). Considering the relative content of the phases in this bulk, excluding the zero solution points, the volume/area percentages of W, CeO_2, Ce_2O_3, and WO_3 were normalized to their total content (83.09 vol.%). After normalization, the volume/area percentages of W, CeO_2, Ce_2O_3, and WO_3 were, respectively, about 90.96 vol.%, 8.26 vol.%, 0.70 vol.%, and 0.08 vol.%. Therefore, it could be calculated that the normalized weight percentages (wt.%) of these phases were, respectively, about 96.45 wt.%, 3.28 wt.%, 0.24 wt.%, and 0.03 wt.%, when the densities of 19.3 g·cm^{-3} for W [37], 7.22 g·cm^{-3} for CeO_2 [37], 6.20 g·cm^{-3} for Ce_2O_3 [37], and 7.20 g·cm^{-3} for WO_3 [37] were brought into the formula of mass and density.
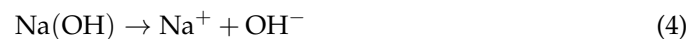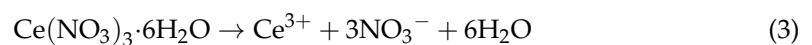
Therefore, it could be obtained that the relative contents of $CeO_2 \cdot 2H_2O$ and $Ce(OH)_3$ in the doped powders were, respectively, about 3.97 wt.% and 0.28 wt.%, as calculated using the formulae shown in Equations (1) and (2). The content of $CeO_2 \cdot 2H_2O$, at about 3.97 wt.%, was much higher than that of $Ce(OH)_3$, which was about 0.28 wt.%. This result agreed well with the designed content of 4 wt.%.

It could also be obtained from the EBSD phase distribution result shown in Figure 6a that WO_3, with a content of about 0.03 wt.%, could be identified in the bulk materials from the doped powders. In contrast, the bulk materials from the undoped powders contained $WO_{2.96}$ at about 2.40 wt.% and WO_3 at about 0.01 wt.%, as determined from the EBSD phase distribution map shown in Figure 6b. This bulk consisted of W (red) at about 86.02 vol.%, $WO_{2.96}$ (aqua, theoretical density 7.14 g·cm^{-3} [38]) at about 5.71 vol.%, WO_3 (green) at about 0.02 vol.%, and zero solution points (gray and dark) at about 8.25 vol.%. Therefore, it could be proposed that the content of WO_x in the bulk from the undoped powders was much higher than that in the sintered bulk from the doped powders. The result verified

the findings shown in Figure 4, which suggested that $CeO_2 \cdot 2H_2O$ generated in the mixed aqueous solution was distributed on the surface of W particles, therefore impeding the oxidation of W particles during the preparation and sintered of the doped powders.

Based on the relative contents of CeO_2 and Ce_2O_3 in the sintered bulk from the doped powders obtained from the EBSD analysis results, the relative contents of H_2O in $CeO_2 \cdot 2H_2O$ and $Ce(OH)_3$ were calculated using Equations (1) and (2) to be, respectively, about 0.69 wt.% and 0.04 wt.%. This indicated that the pyrolysis water from $Ce(OH)_3$ was negligible compared to that from $CeO_2 \cdot 2H_2O$.

In conclusion, based on the results from EBSD and TG/DSC analysis shown in Figures 5 and 6a, it could be proposed that the shells in the doped powders, characterized by a core–shell structure, were mainly composed of $CeO_2 \cdot 2H_2O$. In the present work, the phase composition of the shell was derived from the sequential chemical reactions in the mixed aqueous solution containing $Ce(NO_3)_3 \cdot 6H_2O$, NaOH, and $C_8H_{14}O_4$ etc., as shown in Equations (3)–(6).

$$Ce(NO_3)_3 \cdot 6H_2O \rightarrow Ce^{3+} + 3NO_3^- + 6H_2O \tag{3}$$

$$Na(OH) \rightarrow Na^+ + OH^- \tag{4}$$

$$Ce^{3+} + 3OH^- \rightarrow Ce(OH)_3 \downarrow \tag{5}$$

$$2Ce(OH)_3 + 1/2O_2 + H_2O \rightarrow 2CeO_2 \cdot 2H_2O \downarrow \tag{6}$$

In the present mixed aqueous solution, Ce^{3+} and OH^- ions were derived from the dissolution of cerium nitrate hexahydrate $(Ce(NO_3)_3 \cdot 6H_2O)$ and sodium hydroxide (NaOH), as described by the reactions in Equations (3) and (4). When the pH increased by adding 10%Na(OH) into the mixed aqueous solution (with the final pH controlled within the range of 10.28–12.00), Ce^{3+} formed a $Ce(OH)_3$ deposit according to the reaction shown in Equation (5) [20]. Due to the presence of dissolved oxygen in the solution, $Ce(OH)_3$ was not stable, leading to the inevitable deposition of $CeO_2 \cdot 2H_2O$ according to the reaction shown in Equation (6) [39]. The incomplete reaction shown in Equation (6) led to the existence of a very small amount of $Ce(OH)_3$ in the doped powders, which subsequently transformed into Ce_2O_3 in the sintered bulk, as obtained from Figures 4 and 6a.

In the present work, since NaOH was added into the mixed aqueous solution drop by drop, the supersaturation of OH^- in the solution was not high enough to promote homogeneous nucleation of the reaction products [40,41]. Therefore, the deposits (mainly $CeO_2 \cdot 2H_2O$) nucleated on the surface of W powders suspended in the solution by heterogeneous nucleation [18]. Due to the small nucleation volume at the concave surfaces of solids [40,41], the deposits preferentially nucleated at the pits with concave characteristics on the surface of the W powders (Figure 2b). As a result, the doped powders composed of a core–shell structure powder characterized by W as the core and granules of $CeO_2 \cdot 2H_2O$ as the shell could be obtained.

3.2. Core–Shell Characteristic of the Doped Powders

The evidence of a core–shell structure with W particle as the core and $CeO_2 \cdot 2H_2O$ as the shell of the doped powders was confirmed from the cross-sectional characteristics of a doped particle shown in Figure 7. The distributions of W, Ce, and O elements in Figure 7b–d, corresponding to the particle shown in Figure 7a, demonstrated an almost overlapping annular Ce-rich and O-rich area around the doped particle. This indicated that $CeO_2 \cdot 2H_2O$ was successfully coated on the surface of the W particle, confirming the formation of the core–shell structure with the W particle as the core and $CeO_2 \cdot 2H_2O$ as the shell, prepared by the wet chemical method. The result aligned with the core–shell W–$La(OH)_3$ structure fabricated by one of the wet chemical methods of electroless plating [18].

The successful preparation of the core–shell structure and the uniformity of the shell thickness could also be evaluated by comparing the particle size distribution of the un-doped and doped powders, as shown in Figure 8. The particle size of the doped powders

changed in the direction of the particle size increase compared to the undoped powders, as observed in the comparison between Figure 8a,c. This provided evidence that the core–shell structure was successfully prepared by the wet chemical method. The similar Gamma distribution curves shown in Figure 8a,c, confirmed by the statistical graph of the probability distribution of the Gamma distribution of particle size shown in Figure 8b,c, indicated the uniformity of the shell thickness in the core–shell structure.
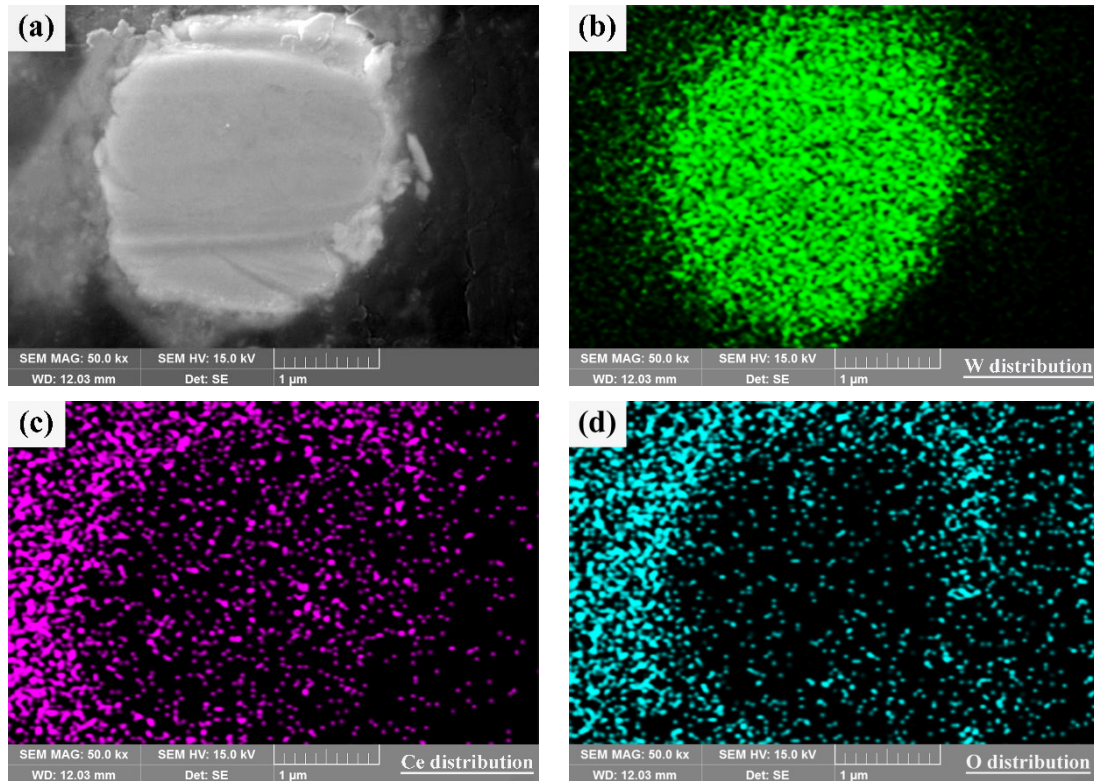
Figure 7. Core–shell structure with W particle as a core and $CeO_2 \cdot 2H_2O$ as a shell of the doped particle: (**a**) cross-section; (**b**–**d**) W, Ce, and O distributions along the cross-section.
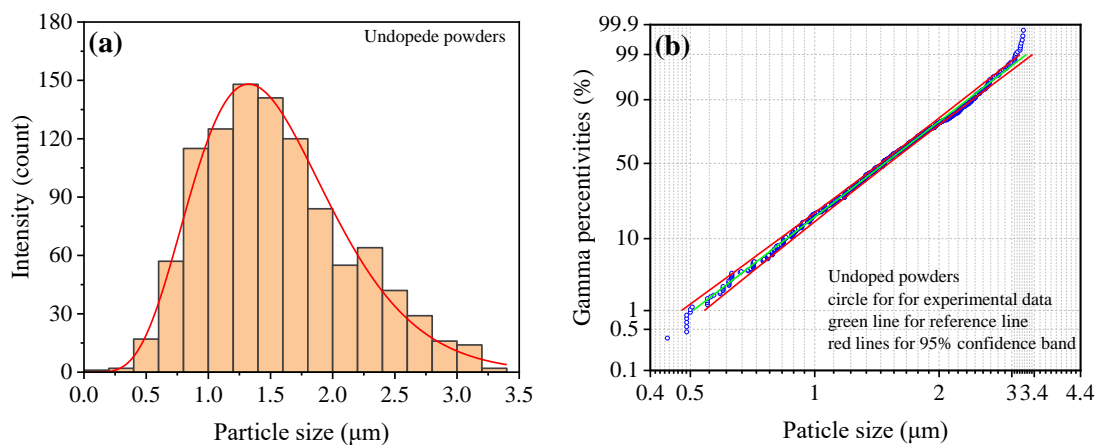
Figure 8. *Cont.*
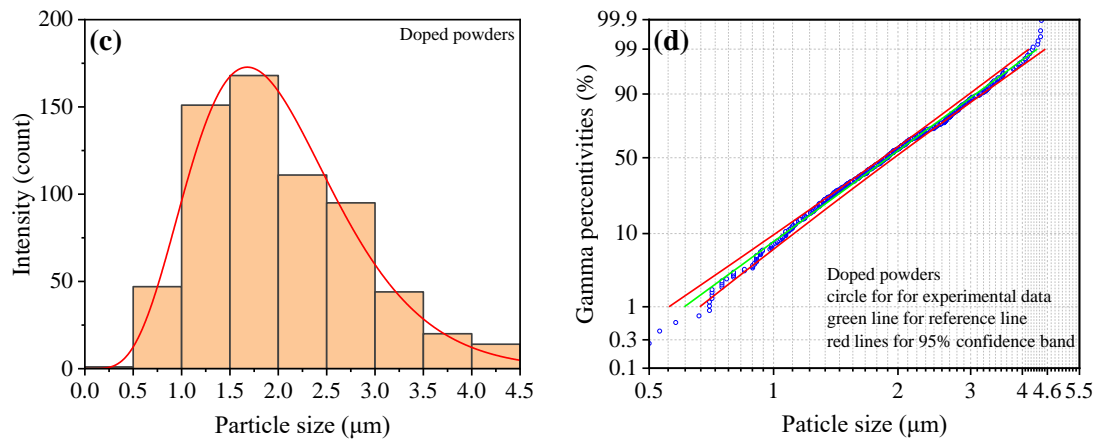
Figure 8. Particle size distribution characteristics and statistical graph of its probability distribution: (**a**,**b**) undoped powders; (**c**,**d**) doped powders.

4. Macroscopic Migration of the Shell Material—From the Perspective of Microstructure Evolution

The macroscopic migration of the shell material during sintering resulted from processes undergone at the microscopic level. In this study, the macroscopic migration characteristics of the shell in the W–CeO$_2$ core–shell system were investigated through the microstructure evolution of the doped powders during sintering at 800–1800 °C. This investigation utilized four adjacent coated powders in a sintered sample of doped powders as the research objects, as shown in Figures 9–13.
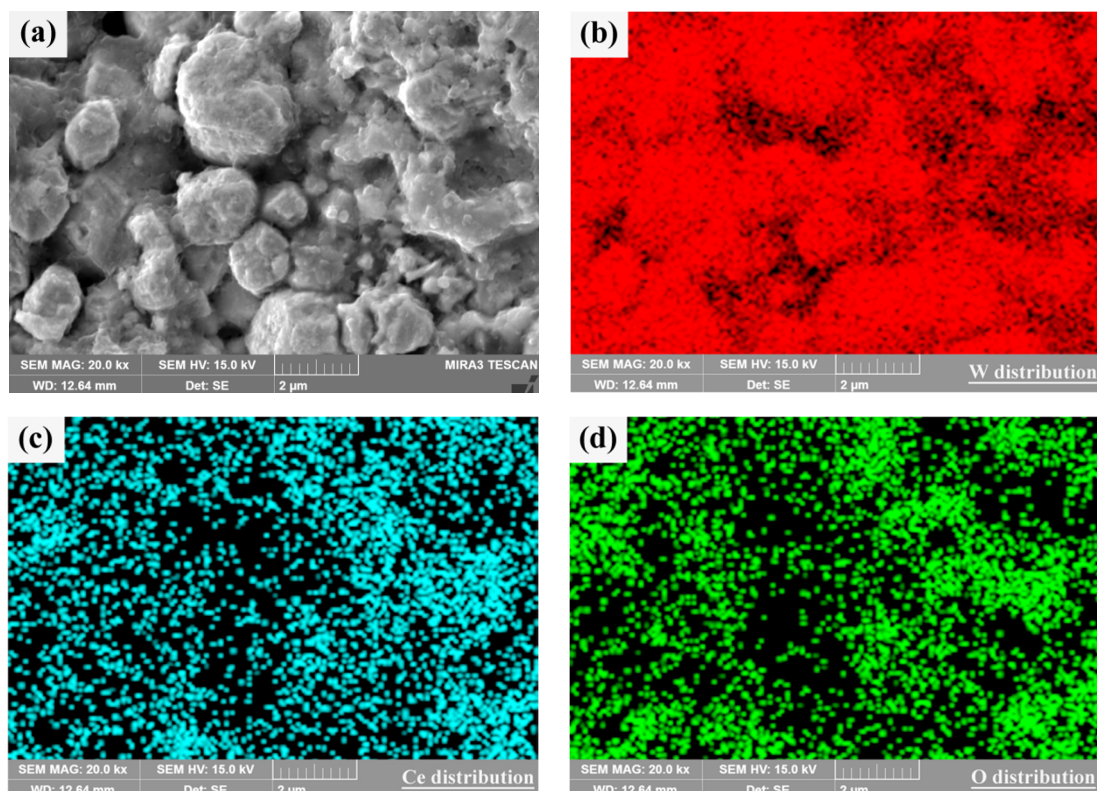
Figure 9. SEM morphology of the core–shell system sintered at 800 °C (**a**) and (**b**–**d**) W, Ce, and O distributions.
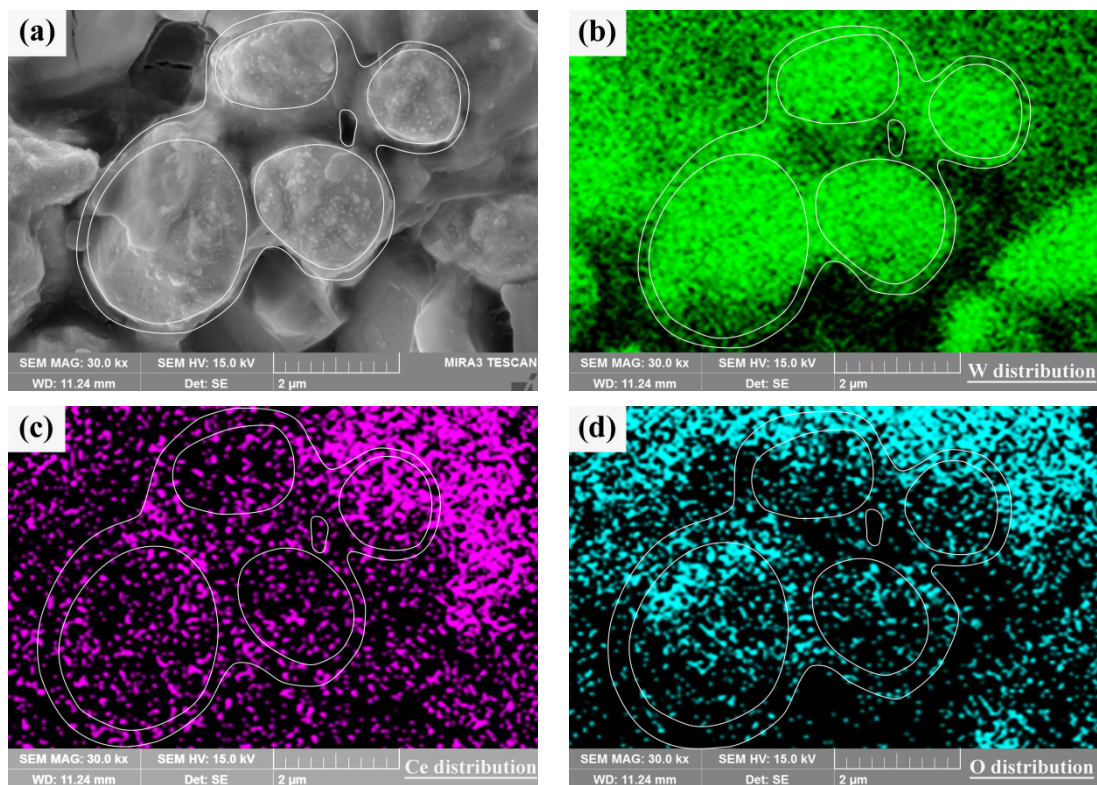
Figure 10. The macroscopic migration characteristics of the shell in the doped powders sintered at 1100 °C indicated by white dotted lines around one selected four adjacent sintered powders where one small pore among the selected four adjacent sintered powders is also delineated by white dashed line: (**a**) SEM morphology; (**b–d**) W, Ce, and O distributions.

Figure 9 shows the typical microstructure of the bulk obtained by sintering the W–CeO$_2$ core–shell system at 800 °C using the sintering process shown in Figure 1b. Compared with the core–shell system before sintering shown in Figure 3a, the microstructure of the core–shell system sintered at 800 °C underwent particle rearrangement and increased particle compaction, as shown in Figure 9a. The surface characteristics of the coated particles before and after sintering at this temperature were similar, as manifested by the presence of obvious sediment characteristics on the surface of the coated particles. This indicated that the shells did not undergo significant macroscopic migration in the core–shell system sintered at 800 °C. The dispersion distribution characteristics of W, Ce, and O elements on the surfaces of the particles further illustrate this point, as shown in Figure 9b–d. Additionally, Figure 9a revealed the presence of noticeable pores between the sintered powders, indicating that the system was in the early stage of sintering when sintered at 800 °C.

When the sintering temperature increased to 1100 °C using the process shown in Figure 1b, obvious sediments around the selected four adjacent sintered powders shown in Figure 10a were observed compared to those obtained at 800 °C (Figure 9a). This indicated that the shell material migrated in the core–shell system when sintered at 1100 °C. The higher grayscale features between the selected four adjacent sintered powders, outlined with white dashed lines in Figure 10a, provided further evidence of the migration of the shell material during sintering at 1100 °C.
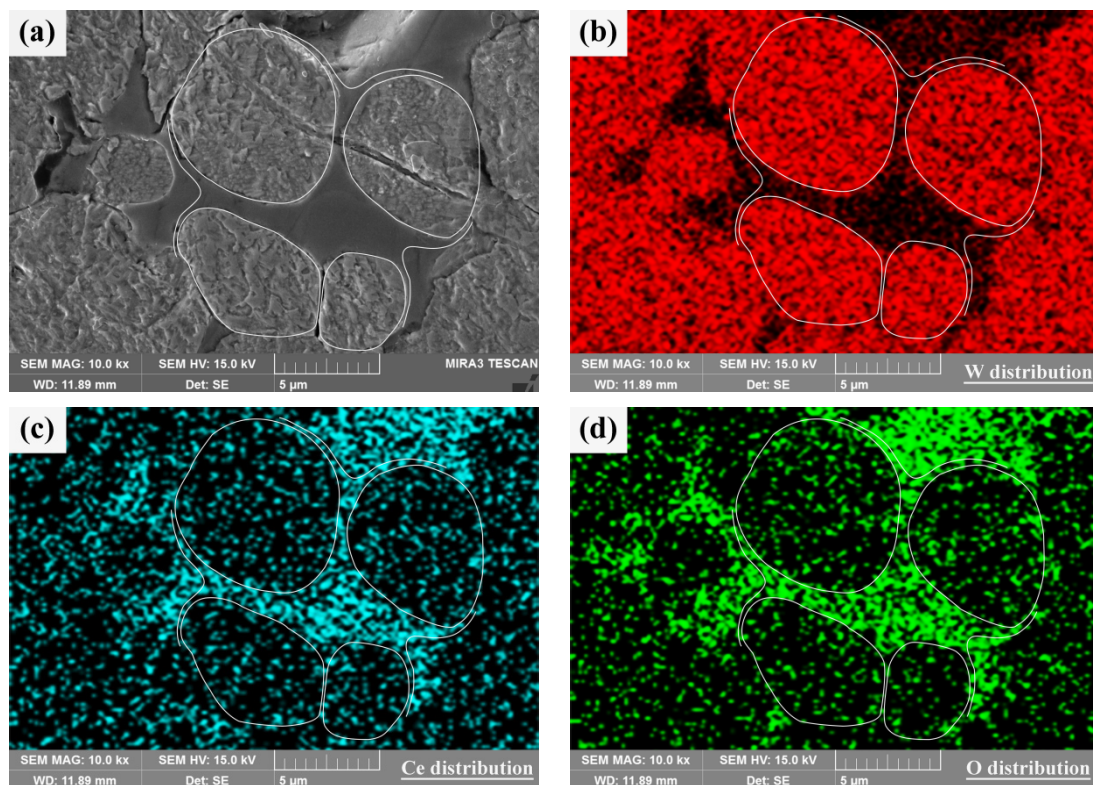
Figure 11. The macroscopic migration characteristics of the shell in the doped powders sintered at 1300 °C indicated by white dotted lines around one selected four adjacent sintered powders: (**a**) SEM morphology; (**b**–**d**) W, Ce, and O distributions.

Further evidence of migration was provided by the distribution characteristics of Ce and O elements around the four adjacent sintered powders, as outlined with white dashed lines in Figure 10c,d. It could be found from Figure 10c,d that the distribution of Ce and O elements around the selected four adjacent sintered powders at 1100 °C was less uniform compared to that at 800 °C, suggesting the migration of shell materials during sintering. In addition, the similarity in the distribution of Ce and O elements around one of the selected four adjacent sintered powders to that between the selected four adjacent sintered powders indicated that the migration of shell materials was likely concentrated around individual doped powders. The migration of shell materials led to the adhesion between two single-doped materials and the formation and growth of sintering necks between two single-doped materials [17,18,42].

It could also be found from Figure 10a that the density of pores in the bulk obtained at 1100 °C was smaller than that in the bulk obtained at 800 °C (Figure 9a), indicating that the migration of the shell material during sintering process helped reduce the porosity of the sintered bulk. One small pore among the selected four adjacent sintered powders was also delineated by white dashed lines, as shown in Figure 10.

It was logical to predict that the migration of the shell material would become more pronounced, and the pores would disappear as the core–shell system was sintered at temperatures above 1100 °C. As could be seen in Figure 11a, when the doped powders were sintered at 1300 °C using the process shown in Figure 1b, the grayscale of the sediments around the selected four adjacent sintered powders, outlined with white dashed lines, was higher than that in the doped powders sintered at 1100 °C using the same process (Figure 10a). The high grayscale areas, rich in Ce and O elements, indicated that the increased sintering temperature facilitated greater migration of shell materials to the areas between the selected four adjacent sintered powders.
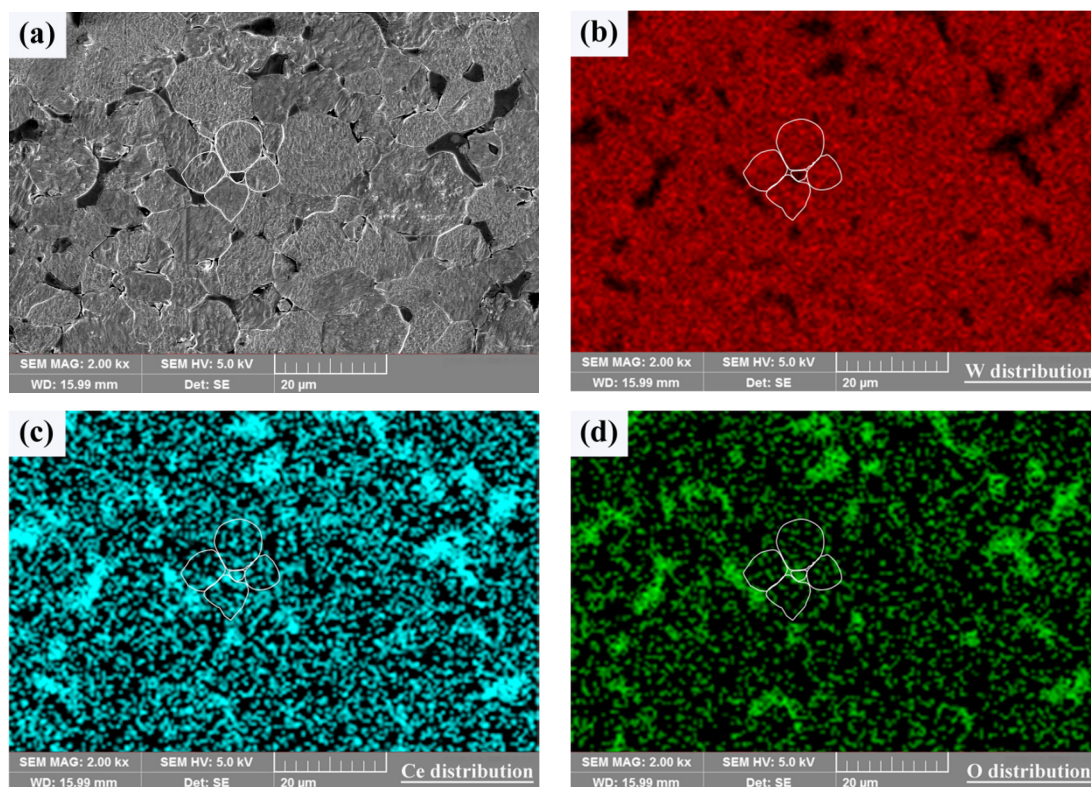
Figure 12. The macroscopic migration characteristics of the shell in the doped powders sintered at 1500 °C indicated by white or white dotted lines around one selected four adjacent sintered powders: (**a**) SEM morphology; (**b**–**d**) W, Ce, and O distributions.

It might also be proposed that the size of the area of Ce and O elements distribution among the selected four adjacent doped powders being larger than those around one of the selected four adjacent sintered powders that the shell materials migrated from around single-doped powders to between the doped powders when sintered at temperatures above 1100 °C. This further indicated that while the shell material migrated when the doped powders were sintered at the lower temperature of 1100 °C, the migration was mainly confined to the vicinity of a single-doped powder. The migration of the shell material among the selected four adjacent doped powders was not yet obvious, resulting in the presence of pores among them, as could be seen in Figure 10a, delineated by small white dashed lines. Additionally, the absence of visible pores among the selected four adjacent doped powders sintered at 1300 °C (Figure 11a) further indicated that the shell materials had migrated among the selected four sintered powders, filling the pores and contributing to improved relative density of the sintered bulk [18].

It could also be seen from Figure 11 that some of the selected sintered powders had sintering necks composed of shell materials between them, while others displayed contact between sintering powders that were free of shell material (core material). The contact between some core materials indicated that sintering had entered the stage of sintering core material. The promotion effect of increasing sintering temperature on the migration of shell materials, as well as the observed trend in shell material migration and the fracture of sintering necks composed of shell materials, were the reasons for the above phenomena [18]. The increase in sintering temperatures to 1500 °C and 1600 °C further illustrated this point, as shown in Figures 12 and 13, where increased contact between more core materials was evident, and shell materials were mainly concentrated between the core materials or at the corners of the two core materials.
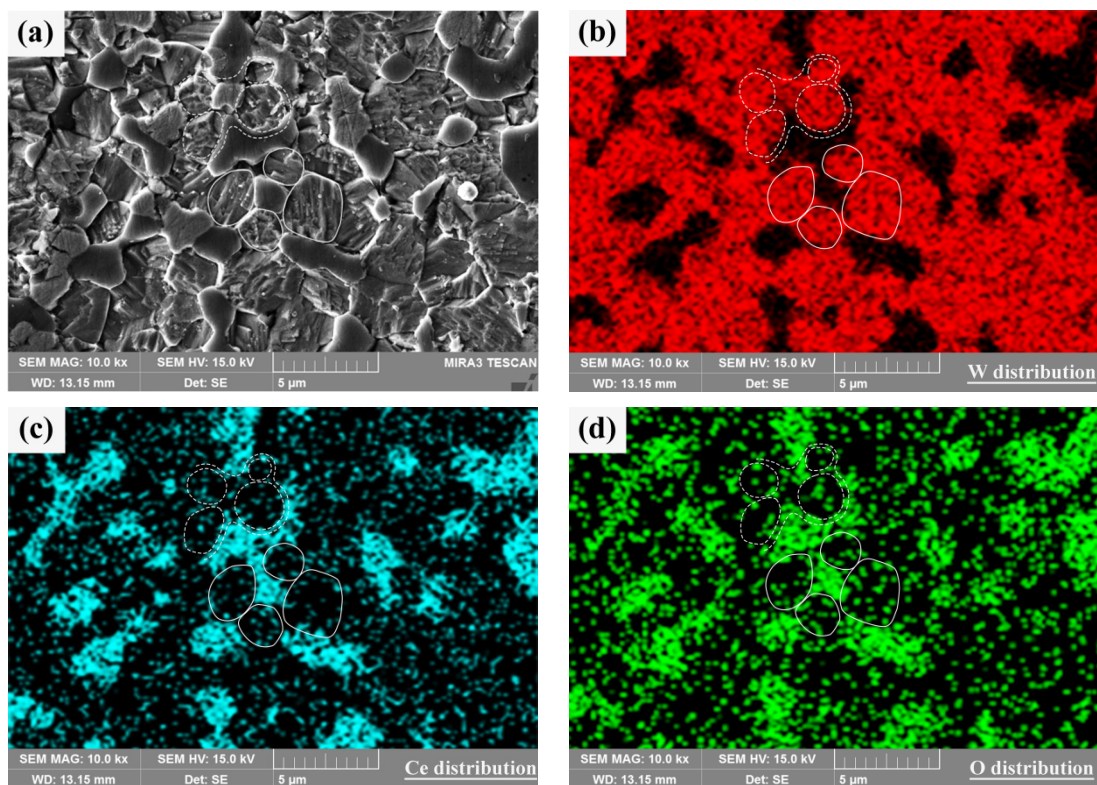
Figure 13. The macroscopic migration characteristics of the shell in the doped powders sintered at 1600 °C indicated by white or white dotted lines around one selected four adjacent sintered powders: (**a**) SEM morphology; (**b**–**d**) W, Ce, and O distributions.

Further increasing the sintering temperature to 1800 °C resulted in the migration of both the core and shell materials, and sintering entered the final stage of forming a dense sintered bulk, as shown in Figure 14a. The dark phase enriched with Ce and O should be CeO_2, which could be verified by the EBSD phase distribution results shown in Figure 6.

Detailed information about the distribution characteristics of CeO_2 and its effect on the microstructure of the bulk prepared by sintering the doped powders at 1800 °C could be provided by the IPF (Inverse Pole Figure) EBSD coloring maps with phase distribution included, as shown in Figure 14. The W grain size was relatively uniform, and there were almost no large areas exhibiting the same color (orientation), suggesting that the texture characteristics were not pronounced.

For comparison, the IPF EBSD coloring maps with phase distribution of the bulk prepared by sintering the undoped powders using the same process were illustrated in Figure 15. Compared with the doped powders sintered bulk at 1800 °C, the grain size of the undoped powders sintered bulk was larger and less uniform, and there were some areas with more concentrated grain orientation.

It could be proposed from Figures 11 and 12 that CeO_2-doped W-based powder was composed of a series of W–CeO_2 core–shell structures formed by the distribution of granular CeO_2 particles around the W particles. To analyze the macroscopic migration characteristics of CeO_2, A system composed of four adjacent core–shell structures was used as the research object. The microstructure evolution of the doped powders sintered at 800–1800 °C is illustrated in Figures 9–13.

The results indicated that the core–shell structure powders rearranged and compacted when sintered at a lower temperature of 800 °C, while CeO_2 and W underwent macroscopic migration at higher temperatures. The macroscopic migration characteristics of CeO_2 with increasing sintering temperature and its effect on the relative density of the sintered bulk could be summarized as follows.
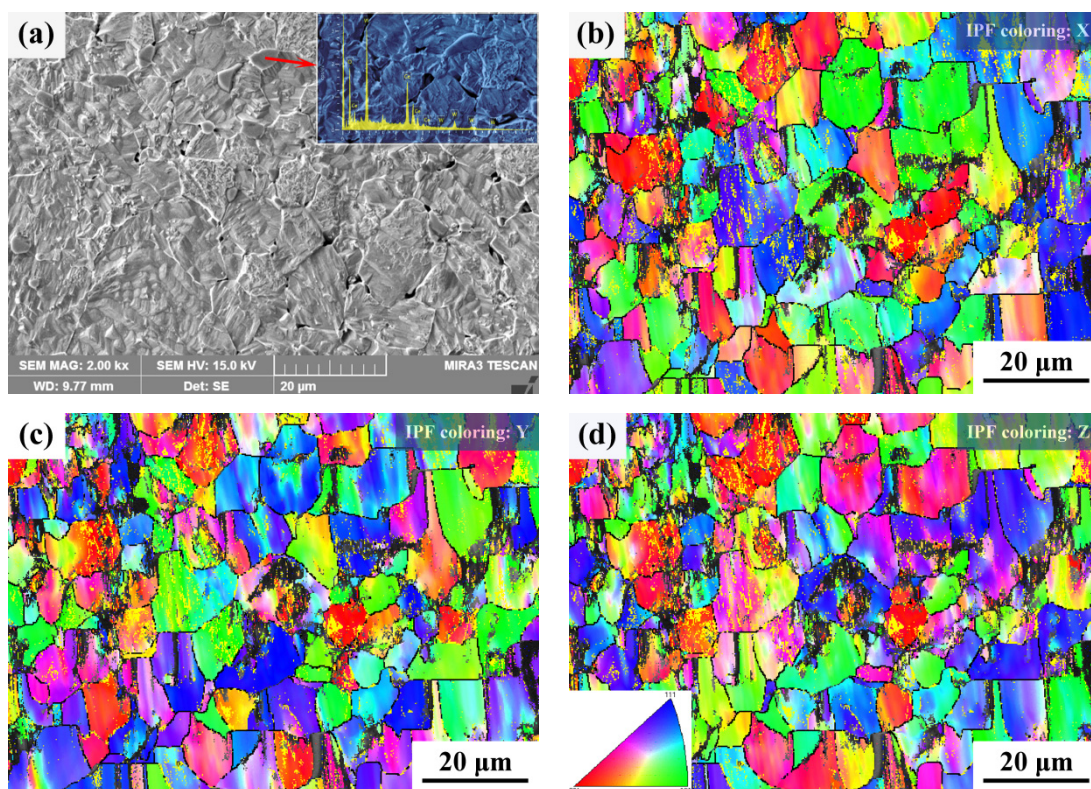
Figure 14. The final microstructure of the doped powders sintered at 1800 °C: (**a**) SEM morphology; (**b**) IPF along X direction; (**c**) IPF along Y direction; (**d**) IPF along Z direction (obtained using an EBSD analysis post-processing software of Channel 5, where the black lines were W grain boundaries, different colors represented different crystal orientations).

CeO_2 first migrated around W particles, initiated the adhesion of CeO_2 particles, and facilitated the formation and growth of sintering necks composed of CeO_2. Meanwhile, CeO_2 also migrated at the contact points between adjacent core–shell structures, resulting in enhanced adhesion between CeO_2 particles at these contacts, followed by the formation and growth of sintering necks composed of CeO_2. This migration of CeO_2 resulted in the disappearance of the granular characteristics of the CeO_2 particles both around the W particles or at the contact points between adjacent core–shell structures.

Then, CeO_2 distributed around the W core migrated towards the contact points between adjacent core–shell structures. This migration facilitated the further growth of sintering necks composed of CeO_2 at these contact points, leading to the elimination of pores between the adjacent core–shell structures.

Finally, CeO_2 continued to migrate, leading to the disappearance of the sintering necks composed of CeO_2 between adjacent W particles. This migration promoted the approach and adherence of the W particles, leading to the formation and growth of sintering necks composed of W material. Therefore, a densified sintered bulk was obtained, with W as the matrix and CeO_2 distributed within the intragranular and grain boundaries of the W.

Therefore, it could be predicted that the migration of CeO_2 during sintering and its distribution characteristics in the sintered bulk were factors that improve the relative density of the bulk sintered from the core–shell structures CeO_2-doped W-based powders, characterized by W particles as the core and CeO_2 as the shell. The result was also confirmed by our previous study [18].

However, as illustrated in Figures 7a and 12c, differences in the size, morphology, and core–shell structure quality of CeO_2-doped W-based powders led to complexities in material migration and sintered densification during sintering. Therefore, as indicated in Figures 9–13, using the microstructure evolution of four adjacent W–CeO_2 core–shell

powder particles at limited sintering temperatures to illustrate the macroscopic migration of CeO_2 and its effect on the densification of the sintered CeO_2-doped W-based bulk was not entirely convincing. In addition, the inevitable inconsistencies in the quality of sample preparation for observing the microstructure between limited sintered bulk materials, as well as the limitations in EDS resolution, were also factors that made the above results not completely convincing.
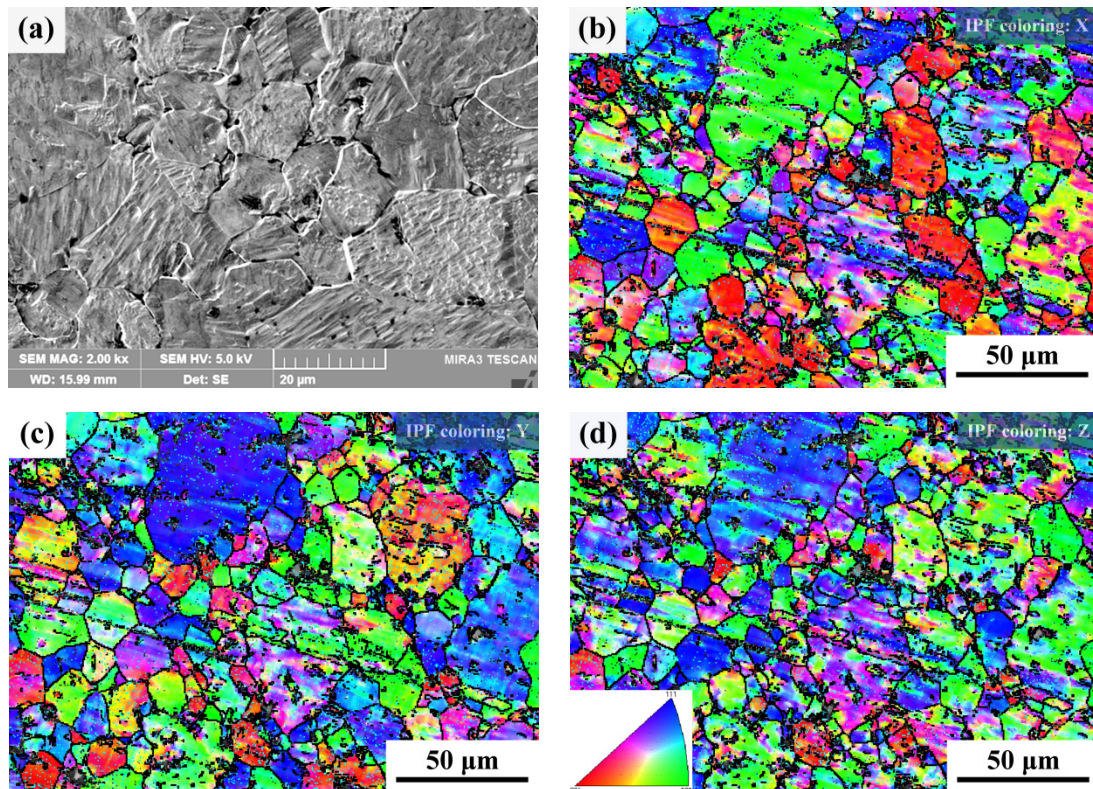

Figure 15. The final microstructure of the undoped powders sintered at 1800 °C: (**a**) SEM morphology; (**b**) IPF along X direction; (**c**) IPF along Y direction; (**d**) IPF along Z direction (obtained using an EBSD analysis post-processing software of Channel 5, where the black lines were W grain boundaries, different colors represented different crystal orientations).

5. Macroscopic Migration Mechanism of the Shell—From the Perspective of Simulation

To avoid the limitations in studying the macroscopic migration of CeO_2 during sintering and its effect on sintering densification due to processes undergoing at the microscopic level shown in Figures 9–13, using finite powder particles with predetermined shapes and sizes as the research object and applying numerical simulation methods. This methodology offered a more effective means to clarify the material migration mechanism during sintering and its effect on sintering densification [43]. In this work, a system comprising four W–CeO_2 core–shell structured powders, all with equal diameters and tangent to each other, was utilized as a model. The migration mechanism of CeO_2 during sintering and its influence on the relative density of CeO_2-doped W-based sintered bulk were analyzed using a combination of ternary phase field and finite-element methods. The simulated results could provide a basis for developing sintering processes and study densification mechanisms for W-based composite powders with a core–shell structure characterized by W as the core and compound as the shell.

5.1. Simulation Method

A ternary phase–field simulation using the Cahn–Hilliard model [44], suitable for studying the evolution of three immiscible phases, was employed used to investigate the

macroscopic migration of the shell in the core–shell system during the initial sintering stage. From a simplification perspective, the focus was primarily on the macroscopic migration of the shell due to the capillary effect, with minimal consideration given to the macroscopic migration of the core material during sintering. In addition, the corresponding relationship between the macroscopic migration of the shell and temperature/time was not considered in the simulation process; it only considered that of the shell and the simulation time steps. The macroscopic migration mechanism of the shell in the core–shell system during the initial sintering stage was proposed by evaluating the relationship between the shell thickness along typical directions and the simulation time steps.

5.2. Model Variables

As obtained from the results shown in Figures 6 and 8, CeO_2 and W were immiscible with each other at sintering temperatures of 1800 °C or below. Additionally, air also could not form a solid solution with W and CeO_2. Consequently, the three phases of vacuum with 10^{-3} Pa air (denoted as phase A), CeO_2 (denoted as phase B), and W (denoted as phase C) were considered immiscible with each other. In this simulation, each phase was described geometrically by a phase–field variable Φ_i (i = A, B, and C), representing the volume concentration of the respective phase [44]. To build the mathematical model, the phase–field variables should satisfy the following three constraints [44].

The first constraint was that the phase–field variable should be thought of as a smooth function, which equals 1 within the i-phase and 0 outside of it, varying continuously at the interfaces between the i-phase and other phases. Assuming the density of each phase was constant, the phase–field variables satisfied the constraint shown in Equation (S1).

The second constraint was that the equations satisfied by the above ternary phase–field variables were formally identical. The third constraint was that the three-phase model should coincide with the two-phase model when only two phases were present (that is, if, for instance, $\Phi_B = 0$ everywhere in the domain).

5.3. Models and Constraints Conditions

In this work, it was assumed that the shell in the core–shell W–CeO_2 structure was represented by a porous film layer composed of fine CeO_2 particles produced by wet chemical reactions and deposited on the surface of W particles. The above ideal two-dimensional model, composed of four W particles with an equal diameter of 2.5 μm and a series of CeO_2 particles with an equal diameter of 0.5 μm closely distributed around them, is shown in Figure S1a. This model featured interfacial areas between the two phases. The mesh with interfacial refinement for the model used in the simulation is shown in Figure S1b. Because a repulsive force existed between two subsystems in a two-phase system at rest, an additional force, namely surface tension (force per unit length in N/m or energy per unit area in J/m^2), which represented the free energy needed to create an interface between two phases, was required to maintain contact between the subsystems [45].

For the three-phase system consisting of W, CeO_2, and a vacuum at 10^{-3} Pa shown in Figure S1, it was logical to predict that most interfacial areas involved only two of the three phases rather than all three during sintering. That was to say that the above-mentioned three constraints for phase–field variables might exist simultaneously but should be considered exceptional [44]. This indicated that in a certain area where only a two-phase interface was present, the third phase effectively became separated from the three-phase system. Achieving such separation required an external force, which was known as additional free energy [45].

According to the relationship between free energy and surface tension, where surface tension represented the free energy needed to create an interface between two contacting phases [45], and the characteristic that surface tension was a force tangent to the surface and normal to the contour separating the two subsystems. Therefore, in the three-phase system without wettability between phases shown in Figure S1, the contact interface between any two phases could be regarded as straight. The required additional free energy

$|\nabla\Phi_i|^2$ when one phase of the three-phase system was separated from the system could be expressed by Equation (S2) [45].

Since the form of Equation (S2) was the same as the relationship between the capillary coefficient ($\sum_i |\nabla\Phi_i|^2$) and the surface tension coefficient of the interface separating one phase from its contact phase [44], if Equation (S2) was satisfied, the first property to ensure the constraint conditions for consistency between the three-phase field and two-phase field was satisfied. That was to say that the free energy of the three-phase was equal to that of the two-phase field model when phase i was absent [44]. In addition, because all three phases were present initially in the three-phase system shown in Figure S1, the second property that phase i must not appear artificially during the evolution of the sintering system when phase i was not present at the initial time to ensure the constraint conditions for consistency between three-phase and the two-phase field was also satisfied.

5.4. Model Construction and Solution

Based on the above constraints, the total free energy (F) of the system in the three-phase field model during sintering could be defined as a function of the phase–field variables in the manner of Equation (S3) (Cahn–Hilliard diffusion equation), which could also be used to solve the two-phase filed issue that arose in the present sintering process [44].

The bulk free energy density function $f(\Phi_A, \Phi_B, \Phi_C)$ was defined by Equation (S4), which probably had no true microscopic physical meaning but could be understood as a phenomenological extrapolation of the diphasic model to the three immiscible situations [44].

For the three-phase system shown in Figure S1, without consideration of the velocity field, the evolution of the order parameter Φ_i (i = A, B, and C) was driven by the generalized chemical potential shown in Equation (S5) [44].

The numerical method adopted here to solve the three-phase field model involved the use of a finite element method (FEM) with adaptive meshing algorithms proposed by Yue et al. [46]. During the FEM analysis, an interpolation function, int (t), was applied to account for the time and temperature history of the simulation. This function controlled the evaluation of the model between discrete points and outside the defined domain, as shown in Figure S2.

In the current three-phase immiscible system, it was assumed that phase transport did not involve convection. This was implemented through a boundary condition termed wetted walls ($\vec{n}_{wall}$). When this boundary condition was applied, the phase interfaces could move along the wall. In the macroscopic migration of the CeO_2 shell in the present three-phase immiscible system, this boundary condition enforced the absence of convection or penetration, as indicated in Equation (S8).

Along the wetted walls, the contact angles of the interfaces from phase A to phase C (θ_α), phase B to phase C (θ_β), and phase A to phase B (θ_γ) were specified to be equal to $\pi/2$ rad, representing no wetting between phases, as could be present in Equation (S9).

In addition, the real correspondence between phase transports and temperature/time during the simulation, as well as the external stress, were also not considered. The macroscopic migration of the CeO_2 shell in the core–shell W–CeO_2 system was only simulated from the perspective of the sequence of time steps and was controlled only by Equation (S3). The thermodynamics parameters used in this simulation were as follows: diffusion mobility (M_o) was $1.5 \times 10^{-5} \exp(-11370/int(t))$ m^3/s; $\sigma_{AB} = \sigma_{BC} = 1.7$ N/m; $\sigma_{AC} = 2.8$ N/m.

5.5. Simulation Results

The macroscopic migration characteristics of the shells in the W–CeO_2 core–shell structure during sintering, simulated using the Cahn–Hilliard ternary phase–field model [44] based on Figure S1 and Equations (S1)–(S9), are shown in Figure 16. The close-packed model was composed of four sets of equal-diameter core–shell structures at the initial time step of the simulation (Figure 16a, t = 0 s) for a subsequent sintering simulation. The red

series represented the cores, the green series represented the porous shell, and the blue series represented the 10^{-3} Pa vacuum.

At the beginning of the simulation (t = 0 s), the equal-diameter doped particles were closely arranged around the core and condensed together. During the early stage of the sintering (t < 9×10^{-4} s), the doped particles in contact with each other migrated along the periphery of the core relatively rapidly, forming sintering necks between the shell particles and growing into a shell around the core–shell structure. As the simulation progressed (t < 1.04×10^{-4} s), continued migration of the core particles led to the formation and growth of sintering necks at the contact points between the four core–shell particles. This migration reduced the porosity between the core–shell structures until the pores disappeared. As the simulation continued (t < 1.22×10^{-4} s), the doped particles continued to migrate, causing the sintering necks composed of doped particles between adjacent core particles to disappear. Ultimately, the core particles approached each other and adhered, leading to the formation and growth of sintering necks composed of the core particles.

Therefore, the evolution of doped powders during the initial sintering process could be divided into seven sequential stages. For simplification, the formation and growth of sintering necks in a four-ball model could be summarized in these seven stages, as shown in Figure 17, where W grain boundaries were represented by solid black lines, W was in the red phase, and CeO_2 was in the yellow phase.

The first stage was the release of water and the formation of sintering necks between CeO_2 particles. When the sintering temperature rose above 279 °C, $Ce(OH)_4$ was converted to CeO_2 and H_2O (g) in situ. Under the influence of surface energy and sintering pressure, adjacent CeO_2 particles came into contact, initiating the formation of sintering necks at their contact points.

The second stage was the growth of the sintering necks between CeO_2 particles and the formation of sintering necks between adjacent CeO_2 shells. The sintering necks between CeO_2 particles continued to grow, forming a shell of CeO_2 particles around each W particle. Concurrently, the diffusion and migration of the CeO_2 shells led to the formation of sintering necks between adjacent CeO_2 shells.

The third stage was the fracture of the sintering necks between the CeO_2 shells and the reduction of porosity between the four core–shell particles. The CeO_2 at the contact points of the four CeO_2 shells further migrated to the center of curvature of the CeO_2 sintering necks, resulting in the fracture of the sintering necks. This migration resulted in a substantial reduction of porosity between the CeO_2 shells.

The fourth stage was the spheroidization of pores between the four core–shell particles. CeO_2 continued to migrate to the pores between the four core–shell particles, causing the pores to gradually take on a spherical shape.

The fifth stage was the disappearance of the pores between the four core–shell particles. CeO_2 further migrated into the pores between the four core–shell particles. This ongoing migration led to the complete elimination of the pores.
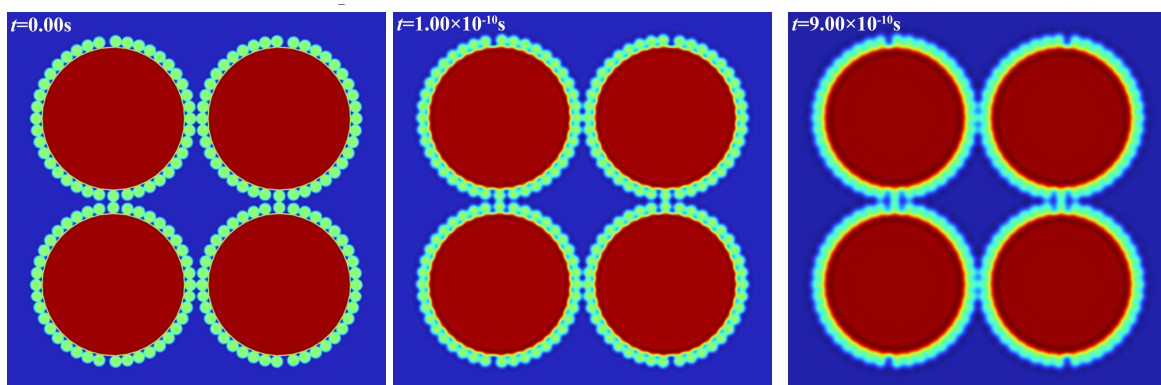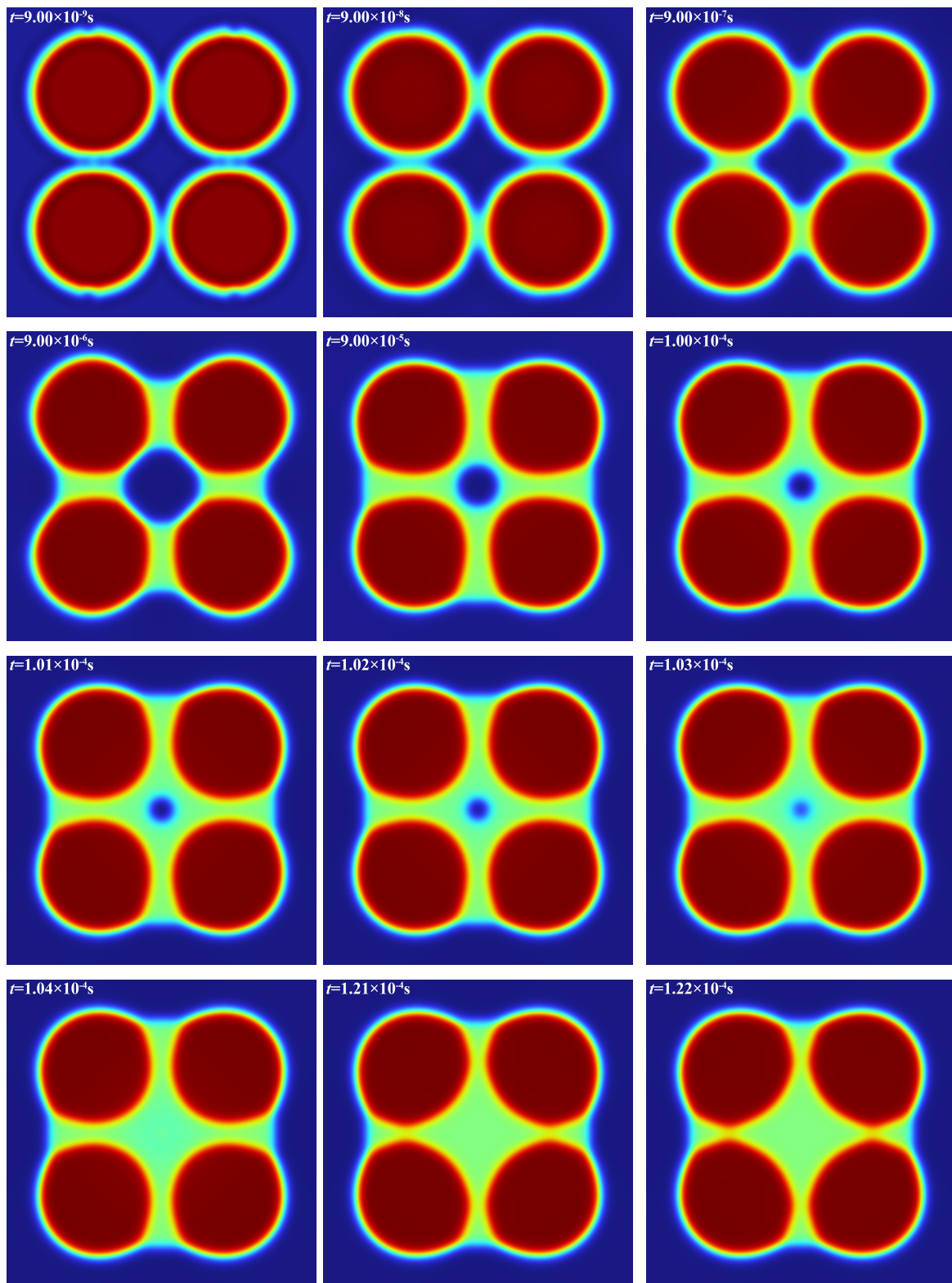

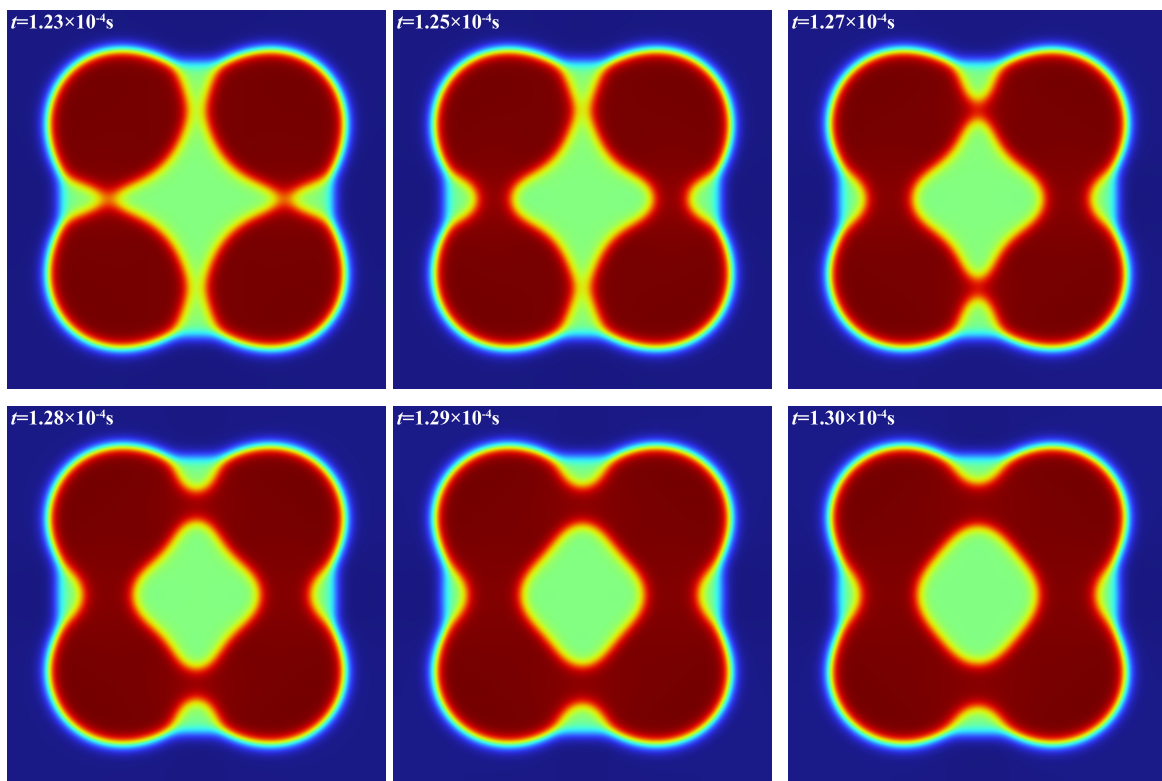**Figure 16.** *Cont.*

Figure 16. *Cont.*

Figure 16. Macroscopic migration characteristics of the shells in the W–CeO$_2$ core–shell structure during the sintering process simulated using the Cahn–Hilliard ternary phase–field model based on Figure 2.
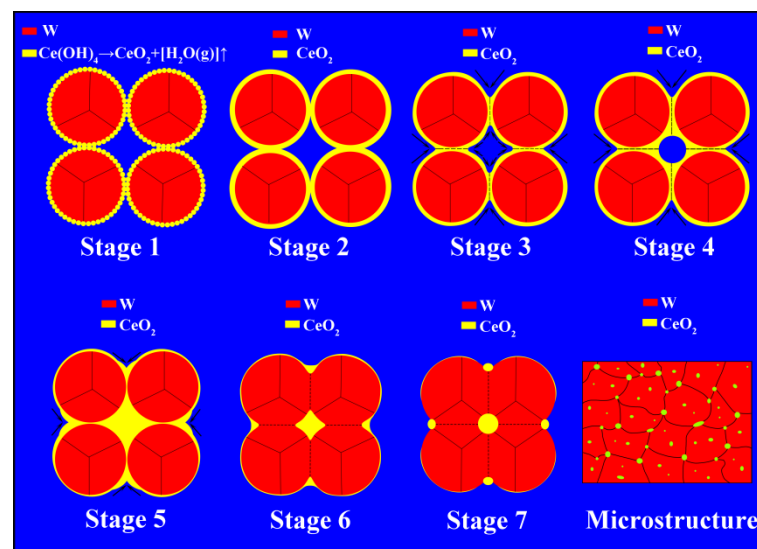

Figure 17. Schematic diagram of the evolution of the sintering necks during the sintering process.

The sixth stage was the contact of the four W particles and the formation of W sintering necks. As the CeO$_2$ shells continued to migrate, the underlying W particles became exposed and made contact with each other. This contact initiated the formation of sintering necks between the W particles. Under the combined influence of diffusion and sintering pressure, the four W particles bonded at these contact points, leading to the formation of W sintering necks.

The seventh stage was the growth of the W sintering necks and spheroidization of CeO$_2$ particles. Under the continued influence of diffusion and sintering pressure, the

W sintering necks grew. Concurrently, the CeO_2 particles underwent spheroidization, Aggregating into more spherical shapes. The spherical CeO_2 particles were distributed in the sintering pores of the four W particles, effectively filling the pores.

For the densification mechanism of doped powder sintering bulk, as mentioned in our previous study [18], the fusion of W particles, the reconstruction of grain boundaries, and the closure of pores occur during the sintering process. In addition, the spheroidization and redistribution of CeO_2 particles. Finally, a sinter bulk with CeO_2 particles distributed at the W grain boundaries and within the grain was obtained.

To further illustrate the migration characteristics of the shell in the W–CeO_2 core–shell structure during the sintering process, the radius variation of the sintering neck in both directions of the four-sphere model was analyzed, as shown in Figure 18. The sintering neck growth during sintering conformed to the formula $(X/D)^n = Bt/D^m$, where X was the radius of the sintering neck, D was the particle diameter, B was the constant related to the material and process, and the values n, m, and B depended on the migration mechanism of the substance. Taking the logarithm on both sides of the above formula yields: $\lg X = (\frac{1}{n}\lg\frac{B}{D^m} + \lg D) + \frac{1}{n}\lg t$, linear fitting of this equation gave n ≈ 2. For this study, n = 2 and m = 1 suggested that the migration mechanism was indicative of viscous flow and plastic flow. Given that the doped power had CeO_2 as the shell, this indicated viscous migration during the sintering process [47]. In addition, it could be seen from Figure 18 that the thickness of the sintering neck in both directions was not synchronized. This discrepancy mainly arose due to the shell, composed of equal-sized particles, did not completely cover the core particles in the four-sphere model used in this study, as shown in Figure 16.
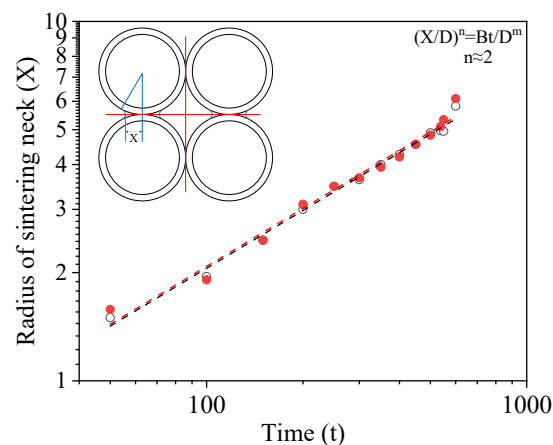

Figure 18. Migration characteristics of the shell in the W–CeO_2 core–shell structure during the sintering process.

6. Conclusions

(1) $CeO_2 \cdot 2H_2O$ was successfully coated on the surface of W particles, forming a core–shell structure with W particles as the core and $CeO_2 \cdot 2H_2O$ as the granular and porous shell, prepared by wet chemical method. The obtained doped powder contained about 3.97% CeO_2, which closely matched the intended design content of 4%.

(2) When sintered at 800 °C, the shell of the core–shell power underwent minimal macroscopic migration, indicative of the early sintering stage. Upon reaching 1100 °C, the shell material began to migrate in the core–shell system, concentrating around individual doped powders. At 1300 °C, some of the sintering powders displayed sintering necks composed of shell materials, while the core materials started to contact and entered their own sintering stage. Upon increasing the sintering temperature to 1800 °C, both the shell and core materials underwent migration, leading to the final stage of sintering and resulting in a dense sintered bulk.

(3) From a simplification standpoint, the formation and growth of the sintering neck in the four-sphere model could be divided into seven stages: water release and sintering neck formation between CeO_2 shell particles; growth of sintering necks between CeO_2 shell particles and formation between adjacent CeO_2 shells; fracture of the sintering necks of CeO_2 shells and reduction of core–shell porosity; pore spheroidization; pore disappearance; contact and sintering neck formation between W particle; and growth of W sintering necks and CeO_2 particles spheroidization.

(4) The variation in the sintering neck radius indicated that the core–shell structure of W–CeO_2 exhibited viscous flow behavior throughout the sintering process.

Supplementary Materials: The following supporting information can be downloaded at: https://www.mdpi.com/article/10.3390/met14080842/s1, Figure S1: Schematic of the four-ball model composed of core–shell W–CeO_2 structure (a) and (b) the unstructured triangular mesh with interfacial refinement (the small balls and the big balls represent, respectively CeO_2 and W, and the others represent 10^{-3} Pa vacuum).; Figure S2: The interpolation function int (t) used for FEM simulation.

Conflicts of Interest: Authors Haitao Yang and Chan Wang were employed by the company Nanjing Iron and Steel Co., Ltd. and Deyang Sanhuan Technology Co., Ltd. The remaining authors declare that the research was conducted in the absence of any commercial or financial relationships that could be construed as a potential conflict of interest.

References

1. Manikandan, R.; Raja Annamalai, A. Tungsten Heavy Alloys Processing via Microwave Sintering, Spark Plasma Sintering, and Additive Manufacturing: A Review. *Processes* **2022**, *10*, 2352. [CrossRef]
2. Coenen, J.; Antusch, S.; Aumann, M.; Biel, W.; Du, J.; Engels, J.; Heuer, S.; Houben, A.; Hoeschen, T.; Jasper, B. Materials for DEMO and reactor applications-boundary conditions and new concepts. *Phys. Scr.* **2016**, *T167*, 014002. [CrossRef]
3. Nogami, S.; Nogami, S.; Fukuda, M.; Rieth, M.; Rieth, M. Mechanical properties of tungsten: Recent research on modified tungsten materials in Japan. *J. Nucl. Mater.* **2021**, *543*, 152506. [CrossRef]
4. Yin, C.; Terentyev, D.; Zhang, T.; Nogami, S.; Antusch, S.; Chang, C.-C.; Petrov, R.H.; Pardoen, T. Ductile to brittle transition temperature of advanced tungsten alloys for nuclear fusion applications deduced by miniaturized three-point bending tests. *Int. J. Refract. Met. Hard Mater.* **2021**, *95*, 105464. [CrossRef]
5. Gaganidze, E.; Chauhan, A.; Schneider, H.-C.; Terentyev, D.; Terentyev, D.; Terentyev, D. Effect of irradiation temperature on the fracture-mechanical behaviour of tungsten irradiated to 1 dpa. *J. Nucl. Mater.* **2021**, *556*, 153200. [CrossRef]
6. Hu, X. Recent progress in experimental investigation of neutron irradiation response of tungsten. *J. Nucl. Mater.* **2022**, *568*, 153856. [CrossRef]
7. Yucheng, W.U. The routes and mechanism of plasma facing tungsten materials to improve ductility. *Acta Metall. Sin.* **2019**, *55*, 171–180.
8. Chen, Z.; Yang, J.; Zhang, L.; Jia, B.; Qin, M. Effect of La_2O_3 content on the densification, microstructure and mechanical property of W-La_2O_3 alloy via pressureless sintering. *Mater. Charact.* **2021**, *175*, 111092. [CrossRef]
9. Yao, G.; Liu, X.; Zhao, Z.; Luo, L.; Cheng, J.; Zan, X.; Wang, Z.; Xu, Q.; Wu, Y. Excellent performance of W-Y_2O_3 composite via powder process improvement and Y_2O_3 refinement. *Mater. Des.* **2021**, *212*, 110249. [CrossRef]
10. Antolak-Dudka, A.; Oleszak, D.; Zielinski, R.; Kulik, T. W-Y_2O_3 composites obtained by mechanical alloying and sintering. *Adv. Powder Technol.* **2021**, *32*, 390–397. [CrossRef]
11. Suman, V.; Maurya, R.S.; Debata, M.; Chaira, D. Effect of Si addition on phase evolution and microstructure in Y_2O_3 dispersed tungsten (W) and W-based alloys synthesized via mechanical alloying and consecutive conventional sintering. *Mater. Today Commun.* **2022**, *31*, 103341. [CrossRef]

12. Dong, Z.; Ma, Z.Q.; Yu, L.M.; Liu, Y.C. Achieving high strength and ductility in ODS-W alloy by employing oxide@W core-shell nanopowder as precursor. *Nat. Commun.* **2021**, *12*, 5052. [CrossRef] [PubMed]

13. Wang, Y.; Wang, M.; Sun, H.; Tang, K.; Xi, X.; Nie, Z. Characterization of W-Er$_2$O$_3$ alloy pre-pared by co-deposition method and spark plasma sintering. *Int. J. Refract. Met. Hard Mater.* **2023**, *114*, 106253. [CrossRef]

14. Dong, Z.; Liu, N.; Ma, Z.; Liu, C.; Guo, Q.; Yamauchi, Y.; Alamri, H.R.; Alothman, Z.A.; Shahriar, A.; Hossain, M.; et al. Synthesis of nanosized composite powders via a wet chemical process for sintering high performance W-Y$_2$O$_3$ alloy. *Int. J. Refract. Met. Hard Mater.* **2017**, *69*, 266–272. [CrossRef]

15. Hu, W.; Dong, Z.; Ma, Z.; Liu, Y. W–Y$_2$O$_3$ composite nanopowders prepared by hydrothermal synthesis method: Co-deposition mechanism and low temperature sintering characteristics. *J. Alloys Compd.* **2020**, *821*, 153461. [CrossRef]

16. Dai, Y.; Lu, P.; Cao, Z.; Campbell, C.T.; Xia, Y. The physical chemistry and materials science behind sinter-resistant catalysts. *Chem. Soc. Rev.* **2018**, *47*, 4314–4331. [CrossRef] [PubMed]

17. Eom, N.; Messing, M.E.; Johansson, J.; Deppert, K. Sintering Mechanism of Core@Shell Metal@Metal Oxide Nanoparticles. *J. Phys. Chem. C* **2021**, *125*, 16220–16227. [CrossRef]

18. Wang, C.; Wang, P.; Hou, Q.Y.; Cui, Z.Q.; Zhang, N.F.; Luo, L.M.; Huang, Z.Y. Microstructure and properties of La$_2$O$_3$-doped tungsten-based bulk material and its densification mechanism during spark plasma sintering process. *Fusion Eng. Des.* **2023**, *188*, 113420. [CrossRef]

19. Grulke, E.; Reed, K.; Beck, M.; Huang, X.; Cormack, A.; Seal, S. Nanoceria: Factors affecting its pro- and anti-oxidant properties. *Environ. Sci. Nano* **2014**, *1*, 429–444. [CrossRef]

20. Abellan, P.; Moser, T.H.; Lucas, I.T.; Grate, J.W.; Evans, J.E.; Browning, N.D. The formation of cerium(III) hydroxide nanoparticles by a radiation mediated increase in local pH. *RSC Adv.* **2017**, *7*, 3831–3837. [CrossRef]

21. Tok, A.I.Y.; Boey, F.Y.C.; Dong, Z.; Sun, X.L. Hydrothermal synthesis of CeO$_2$ nano-particles. *J. Mater. Process. Technol.* **2007**, *190*, 217–222. [CrossRef]

22. Huang, Y.; Cai, Y.; Qiao, D.; Liu, H. Morphology-controllable synthesis and characterization of CeO$_2$ nanocrystals. *Particuology* **2011**, *9*, 170–173. [CrossRef]

23. Moulder, J.F.; Stickle, W.F.; Sobol, P.E.; Bomben, K.D. *Handbook of X-ray Photoelectron Spectroscopy: A Reference Book of Standard Spectra for Identification and Interpretation of XPS Data*; Physical Electronics, Inc.: Eden Praire, MI, USA, 1995.

24. Subramanian, N.D.; Moreno, J.; Spivey, J.J.; Kumar, C. Copper Core-Porous Manganese Oxide Shell Nanoparticles. *J. Phys. Chem. C* **2011**, *115*, 14500–14506. [CrossRef]

25. Amarjargal, A.; Tijing, L.D.; Im, I.-T.; Kim, C.S. Simultaneous preparation of Ag/Fe$_3$O$_4$ core–shell nanocomposites with enhanced magnetic moment and strong antibacterial and catalytic properties. *Chem. Eng. J.* **2013**, *226*, 243–254. [CrossRef]

26. Liu, S.; Wang, H.; Wei, Y.; Zhang, R. Core-shell structure effect on CeO$_2$ and TiO$_2$ supported WO$_3$ for the NH$_3$-SCR process. *Mol. Catal.* **2020**, *485*, 110822. [CrossRef]

27. Balasubramanian, M.; Melendres, C.A.; Mansour, A.N. X-ray absorption spectroscopy study of the local structure of heavy metal ions incorporated into electrodeposited nickel oxide films. *J. Electrochem. Soc.* **1999**, *146*, 607–614. [CrossRef]

28. Balasubramanian, M.; Melendres, C.A.; Mansour, A.N. An X-ray absorption study of the local structure of cerium in electrochemically deposited thin films. *Thin Solid Film.* **1999**, *347*, 178–183. [CrossRef]

29. Izaki, M.; Saito, T.; Chigane, M.; Ishikawa, M.; Katayama, J.I.; Inoue, M.; Yamashita, M. Low temperature deposition of cerium dioxide film by chemical reaction. *J. Mater. Chem.* **2001**, *11*, 1972–1974. [CrossRef]

30. Haijiang, W.; Jiantang, L. Characterization and electrochemical corrosion behavior of cerium conversion coating on hot-dip galvanized steel. *Chin. J. Nonferrous Met.* **2011**, *21*, 1009–1015.

31. Kobayashi, Y.; Fujiwara, Y. Chemical deposition of cerium oxide thin films on nickel substrate from aqueous solution. *J. Alloys Compd.* **2006**, *408–412*, 1157–1160. [CrossRef]

32. Pardo, A.; Merino, M.C.; Arrabal, R.; Viejo, F.; Muñoz, J.A. Ce conversion and electrolysis surface treatments applied to A3xx.x alloys and A3xx.x/SiCp composites. *Appl. Surf. Sci.* **2007**, *253*, 3334–3344. [CrossRef]

33. Xie, F.Y.; Gong, L.; Liu, X.; Tao, Y.T.; Zhang, W.H.; Chen, S.H.; Meng, H.; Chen, J. XPS studies on surface reduction of tungsten oxide nanowire film by Ar+ bombardment. *J. Electron Spectrosc. Relat. Phenom.* **2012**, *185*, 112–118. [CrossRef]

34. Bouvard, O.; Krammer, A.; Schüler, A. In situ core-level and valence-band photoelectron spectroscopy of reactively sputtered tungsten oxide films. *Surf. Interface Anal.* **2016**, *48*, 660–663. [CrossRef]

35. Bussolotti, F.; Lozzi, L.; Passacantando, M.; La Rosa, S.; Santucci, S.; Ottaviano, L. Surface electronic properties of polycrystalline WO$_3$ thin films: A study by core level and valence band photoemission. *Surf. Sci.* **2003**, *538*, 113–123. [CrossRef]

36. Hughes, A.E.; Taylor, R.J.; Hinton, B.R.W.; Wilson, L. XPS and SEM characterization of hydrated cerium oxide conversion coatings. *Surf. Interface Anal.* **1995**, *23*, 540–550. [CrossRef]

37. Weast, R. *CRC Handbook of Chemistry and Physics*; CRC Press: Boca Raton, FL, USA, 2010.

38. Gebert, E.; Ackermann, R.J. Substoichiometry of tungsten trioxide; the crystal systems of WO$_{3.00}$, WO$_{2.98}$, and WO$_{2.96}$. *Inorg. Chem.* **1966**, *5*, 136–142. [CrossRef]

39. Yu, P.; O'Keefe, T.J. The phase stability of cerium species in aqueous systems III. the Ce(III/IV)-H$_2$O-H$_2$O$_2$/O$_2$ systems dimeric Ce(IV) species. *J. Electrochem. Soc.* **2006**, *153*, C80–C85. [CrossRef]

40. Shamsuddin, M. *Physical Chemistry of Metallurgical Processes*, 2nd ed.; Springer Cham: Berlin/Heidelberg, Germany, 2021.

41. Free, M.L. *Hydrometallurgy: Fundamentals and Applications*, 2nd ed.; Springer: Berlin/Heidelberg, Germany, 2022.

42. Zhang, R.-J.; Chen, Z.-W.; Fang, W.; Qu, X.-H. Thermodynamic consistent phase field model for sintering process with multiphase powders. *Trans. Nonferrous Met. Soc. China* **2014**, *24*, 783–789. [CrossRef]

43. Cheng, Q.; Wang, Y.; Zhang, J.; Conejo, A.N.; Liu, Z. The grain growth and grain boundary migrations during solid-phase sintering of Fe_2O_3: Experiments and simulations. *Chem. Eng. Sci.* **2022**, *262*, 118038. [CrossRef]

44. Boyer, F.; Lapuerta, C.; Minjeaud, S.; Piar, B.; Quintard, M. Cahn–Hilliard/Navier–Stokes Model for the Simulation of Three-Phase Flows. *Transp. Porous Media* **2010**, *82*, 463–483. [CrossRef]

45. Marchand, A.; Weijs, J.H.; Snoeijer, J.H.; Andreotti, B. Why is surface tension a force parallel to the interface? *Am. J. Phys.* **2011**, *79*, 999–1008. [CrossRef]

46. Yue, P.; Zhou, C.; Feng, J.J.; Ollivier-Gooch, C.F.; Hu, H.H. Phase-field simulations of interfacial dynamics in viscoelastic fluids using finite elements with adaptive meshing. *J. Comput. Phys.* **2006**, *219*, 47–67. [CrossRef]

47. Tianshu, Z.; Hing, P.; Huang, H.; Kilner, J. Early-stage sintering mechanisms of Fe-doped CeO_2. *J. Mater. Sci.* **2002**, *37*, 997–1003. [CrossRef]